Korean J. Chem. Eng., 38(4), 653-673 (2021)
DOI: 10.1007/s11814-020-0730-z

pISSN: 0256-1115
eISSN: 1975-7220

INVITED REVIEW PAPER

Porphyrinic zirconium metal-organic frameworks: Synthesis and applications for adsorption/catalysis

Kwangsun Yu*, Dong-Il Won, Wan In Lee**, and Wha-Seung Ahn*,†**

*Department of Chemical Engineering, Inha University, Incheon 22201, Korea
**Department of Chemistry, Inha University, Incheon 22201, Korea
(*Received 16 October 2020 • Revised 3 December 2020 • Accepted 13 December 2020*)

Abstract−Zr-based porphyrinic MOFs, which have isolated porphyrin units imbedded in MOFs' rigid structure, exhibit excellent textural properties and high stability. Among the porphyrin ligands, tetrakis(4-carboxyphenyl)-porphyrin (TCPP) is broadly employed, and so far, seven Zr-based porphyrinic MOFs of MOF-525, MOF-545 (also named PCN-222), PCN-221, PCN-223, PCN-224, PCN-225, and NU-902 have been synthesized using TCCP. The built-in TCPP ligand with various functionality and coordinatively unsaturated Zr clusters can be subjected to diverse pre- and post-synthesis functionalization or guest encapsulation. Aided by the excellent hydrothermal/chemical stability and high porosity, these Zr-based porphyrinic MOFs are gaining attention for applications in adsorption, sensors, heterogeneous catalysis for chemical conversions, photocatalysis, electrocatalysis, and others. This paper reviews the current status of research and development on the synthesis, characterization, functionalization, and adsorption/catalysis applications of Zr-based porphyrinic MOFs.

Keywords: Zr-based Porphyrinic MOFs, Synthesis, Functionalization, Adsorption, Heterogeneous Catalysis

INTRODUCTION

Metal-organic frameworks (MOFs) are a class of crystalline hybrid materials in which metal ions or clusters are interconnected with polydentate organic ligands to form well-ordered one, two, or three-dimensional structures. These are usually synthesized via a solvothermal route in the presence of a deprotonating solvent such as *N,N′*-dimethylformamide (DMF) or hydrothermally in water, using a suitable combination of the metal and organic ligand precursors, which may take several hours to days to complete the synthesis by electrical heating [1]. Owing to their crystallinity with high metal content, high porosity with a large surface area, and various functionality incorporated into the frameworks by both pre- and post-synthetic modifications [2], MOFs have been actively investigated for gas storage [3], separation [4], catalysis [5], sensors [6], and drug delivery [7]. Extensive review articles on their synthesis, characterization, and application are available [8-10].

Among the MOFs, those constructed from high-valent metal ions (Zr^{4+}, Al^{3+}, Fe^{3+}, and Cr^{3+}) and organic carboxylate ligands are important for practical applications due to their high hydrothermal stability derived from the strong coordination bonding formed between the hard Lewis acidic metal ions and hard Lewis basic carboxylates [11,12]. The most commonly studied high stability MOFs are UiO-66 (Zr^{4+}) [13] and MIL-101 (Al^{3+}, Fe^{3+}, or Cr^{3+}) [14] composed of metal clusters and terephthalic acid as shown in Fig. 1.

Porphyrins are frequently used in coordination chemistry owing to their easy complex formation on its N-bonding sites. The metalloporphyrins offer a broad range of optoelectronic and catalytic capabilities and are well known for their biomimetic catalysis [15-17]. Taking advantage of porphyrins' useful properties, many porphyrinic MOFs have been recently synthesized with different porphyrin ligands as shown in Fig. 2 and 3 [18-23]. The porphyrinic

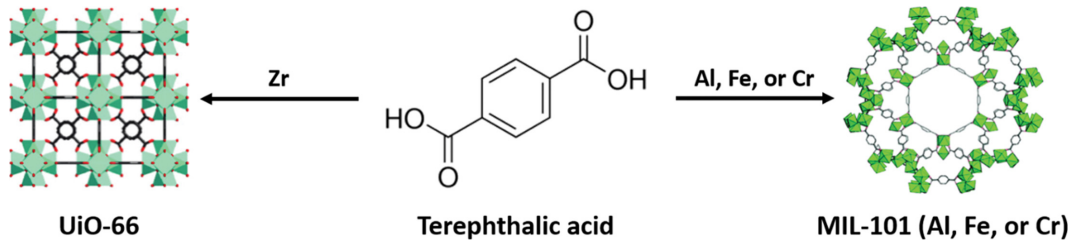

Fig. 1. MOFs with high hydrothermal stability: UiO-66 and MIL-101.

†To whom correspondence should be addressed.
E-mail: whasahn@inha.ac.kr

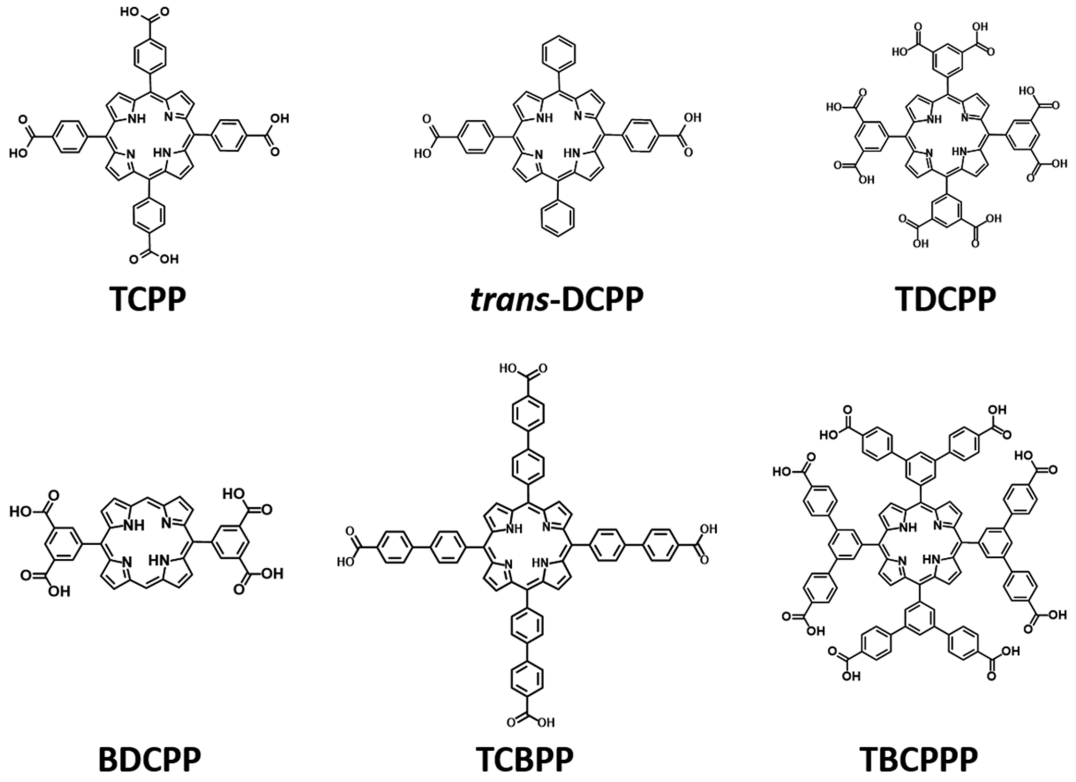

Fig. 2. Representative carboxyphenyl porphyrin ligands for MOFs.

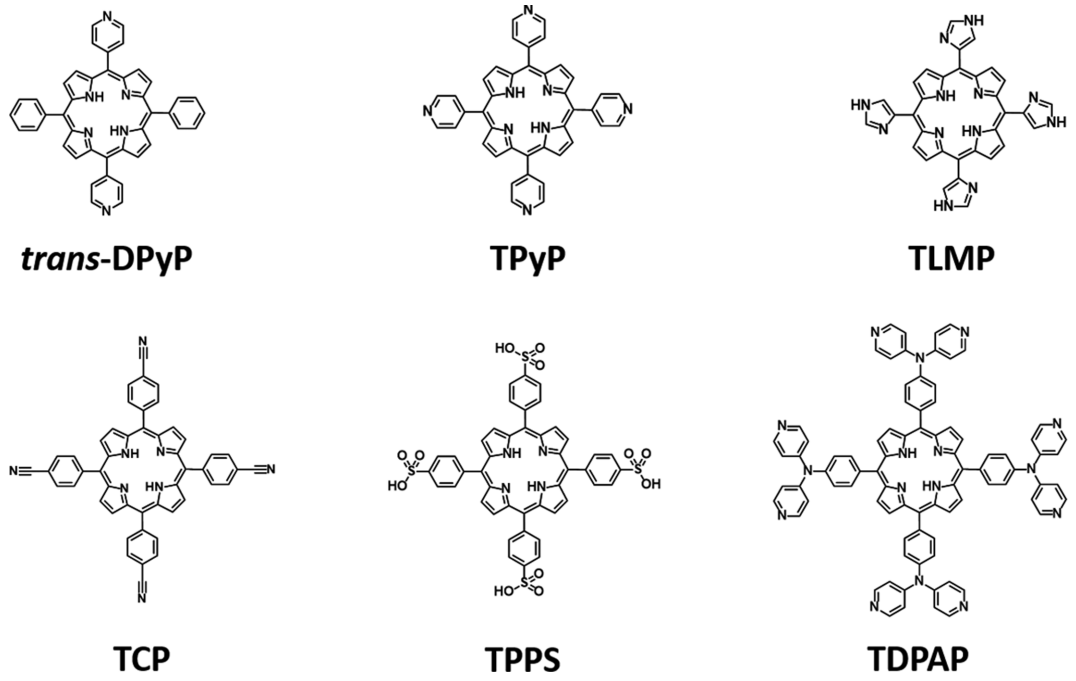

Fig. 3. Representative pyridine and other porphyrin ligands for MOFs.

MOFs have well-separated porphyrin units that can function as active sites for catalysis, adsorption, etc. The porphyrin dimerization, often causing deactivation in the homogeneous porphyrin catalytic/adsorptive system, is avoided by the MOFs' rigid structure [24].

Among the various porphyrin ligands, tetrakis(4-carboxyphenyl)-porphyrin (TCPP) is broadly employed to synthesize a stable porphyrinic MOF composed of metal ions of Zr, Cu, Mn, In, Al, or Fe [25]. In particular, Zr-based porphyrinic MOFs, owing to their excellent textural property and high stability, are drawing atten-

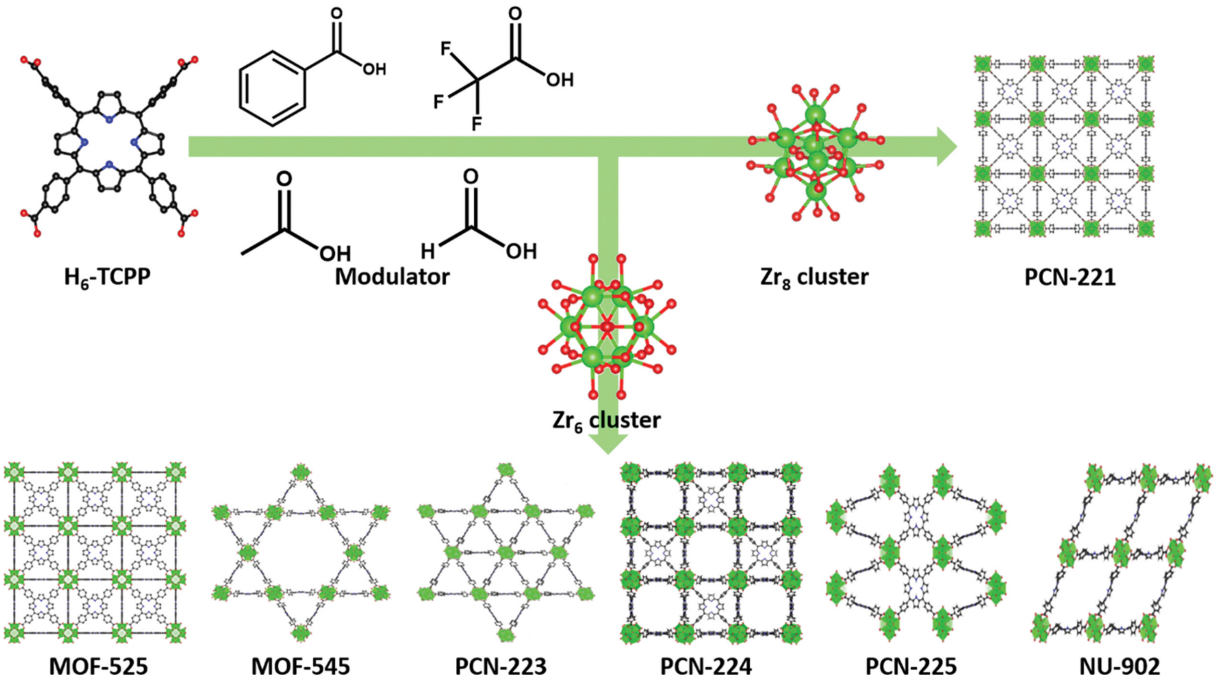

Fig. 4. Zr-based porphyrinic MOFs prepared using TCPP. Green, black, red, and blue spheres indicate Zr, C, O, and N atoms, respectively. H atoms are omitted for clarity. MOF-545 (also named PCN-222 or MMPF-6(Fr)).

tion. The Zr-based porphyrinic MOFs of MOF-525, MOF-545 (also named PCN-222 or MMPF-6(Fr)), PCN-221, PCN-223, PCN-224, PCN-225, and NU-902 have been reported for applications in adsorption and catalysis (PCN stands for Porous Coordination Network, MMPF: Metal-Metalloporphyrin Frameworks, and NU: Northwestern University) [26-30].

As shown in Fig. 4, these Zr-based porphyrinic MOFs in different topologies are synthesized using the same Zr metal precursor and TCPP under a similar set of solvothermal synthesis conditions. Essentially, it is the role of the chemical additive, called modulator, which makes it possible to lead to a different MOF product by controlling the crystallization process aided by their flexible coordination bonding [31]. However, MOF synthesis often produces crystals with two or more mixed morphologies [32], and a careful examination of the synthesis parameters and their optimization is necessary [33-35]. Despite the MOFs synthesis challenges, these Zr-based porphyrinic MOFs are being reported for expanding applications in various areas, especially in adsorption and heterogeneous catalysis.

In this work, we report on the recent progress made on the

Table 1. Synthesis and characterization of Zr-based porphyrinic MOFs reported

	Topology	Synthesis conditions			Textural property				Metalation/ Structural formula	Ref.
		Temp. (°C)	Time (h)	Modulator	S_{BET} (m^2/g)	V_{pore} (cm^3/g)	Pore size (nm)	N_2-Isotherm type		
MOF-525	**ftw**	65	72	Acetic acid	2,620	1.4	2.0	I	Cu, Fe $C_{144}H_{82}N_{12}O_{32}Zr_6$	[49]
MOF-545	**csq**	130	72	Formic acid	2,260	1.6	2.0/3.6	IV	Cu, Fe $C_{96}H_{68}N_8O_{32}Zr_6$	[49]
PCN-221	**ftw**	120	12	Acetic acid, trifluoroacetic acid, or benzoic acid	1,936	0.8	-	I	Cu, Fe, Co $C_{144}H_{78}N_{12}O_{30}Zr_8$	[50]
PCN-223	**shp**	100/ 120	12	Acetic acid or benzoic acid	1,600	0.6	1.2	I	Fe $C_{144}H_{78}N_{12}O_{24}Zr_6$	[51]
PCN-224	**she**	120	24	Benzoic acid	2,600	1.6	1.9	I	Ni, Co, Fe $C_{144}H_{78}N_{12}O_{64}Zr_{12}$	[52]
PCN-225	**sqc**	120	12	Acetic acid	1,902	-	-	I	Zn $C_{48}H_{34}N_4O_{16}Zr_3$	[53]
NU-902	**scu**	90	48	Benzoic acid	2,150	-	1.2/3.0	I	Zn $C_{96}H_{68}N_8O_{32}Zr_6$	[45]

synthesis and applications of the Zr-based porphyrinic MOFs in five sections: (1) synthesis, (2) characterization, (3) functionalization, (4) adsorption, and (5) catalysis. This short review will provide a bird's eye view on the preparation and potentials of Zr-based porphyrinic MOFs for future energy and environmental research applications.

SYNTHESIS

Zr-based porphyrinic MOFs are synthesized solvothermally in DMF or diethylformamide (DEF) using a Zr metal source (zirconium chloride or zirconyl chloride octahydrate), D_{4h}-symmetric TCPP as a porphyrin source (Fig. 2), and an acid modulator. Seven Zr-based porphyrinic MOFs have so far been reported, as shown in Fig. 4 in different topologies derived from the Zr_6 or Zr_8 clusters formed during the synthesis (see Table 1): Zr_6 clusters can have 6 (PCN-224), 8 (MOF-545, PCN-225, and NU-902), or 12 (MOF-525 and PCN-223) connectivity, whereas Zr_8 clusters show 12 (PCN-221) connectivity. The addition of a specific acid modulator is critical to induce a particular topology via controlling the ligand exchange with TCPP during the synthesis (see Fig. 5). The substrate mixture is heated under different temperature and time for a targeted Zr-based porphyrinic MOF.

Low crystallinity or agglomeration of the MOF crystals is commonly observed without a modulator in the Zr-based porphyrinic MOF synthesis, since high charge density of Zr^{4+} polarizes the Zr-O bond to impart covalent character and prohibits the ligand exchange reaction between Zr clusters and the ligands [36]. During the synthesis of Zr-based porphyrinic MOFs, therefore, an acid modulator is usually introduced that competes against TCPP ligand to coordinate with the Zr clusters and slows the nucleation rate. Overall, the acid modulator can produce the following effects: (1) direct guide of framework assembly to a pure phase MOF structure in high crystallinity, (2) particle size control, and (3) defect site formation [37,38]. Several acid modulators, including acetic acid (pK_a=4.75), formic acid (pK_a=3.75), benzoic acid (pK_a=4.20), trifluoroacetic acid (pK_a=0.23), and others have been used. Both the amount and pK_a value of a modulator and synthesis temperature are crucial to achieve high purity and crystallinity of the Zr-based porphyrinic MOFs.

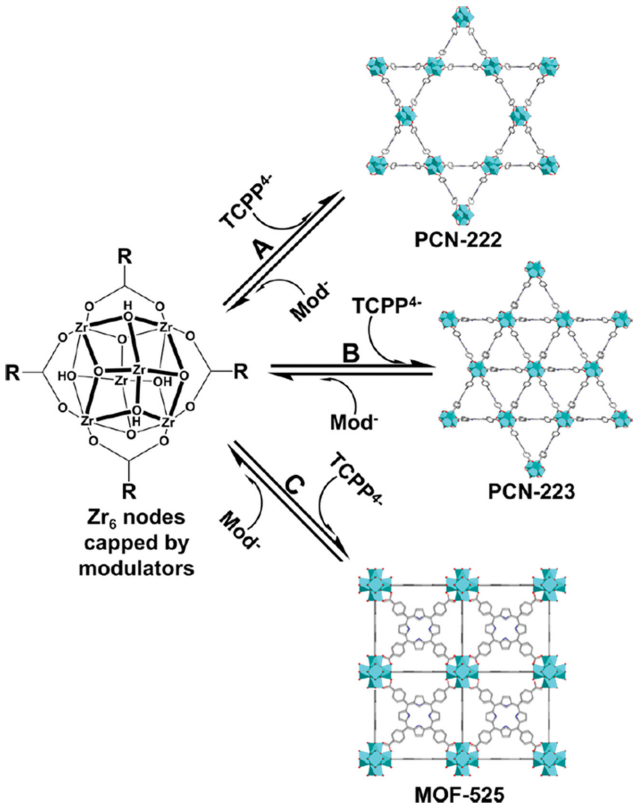

Fig. 5. The equilibrium synthesis mechanism of Zr-based porphyrinic MOFs by deprotonated ligands and modulators. Adapted from Ref. [38] with permission from copyright holders.

Table 1 shows the typical synthesis conditions and the modulator used for different Zr-based porphyrinic MOFs. Rigorous efforts, such as high-throughput synthesis [33], seed-mediated synthesis [39], modulator selection [38], and kinetic and thermodynamic control [40], have been reported to obtain a pure phase Zr-based porphyrinic MOF. Innovations for the synthetic processes are still on-going.

High-throughput synthesis of nanoscale MOF-525, MOF-545, and PCN-223 was reported by Harris et al [33]. To find the optimum synthesis conditions, a total of 1036 synthesis reactions were conducted with different combinations of Zr metal source (zirconium chloride or zirconyl chloride octahydrate), acid modulator (acetic acid, benzoic acid, formic acid, or dichloroacetic acid), synthesis temperature (90, 120, or 130 °C), synthesis time (18 or 72 h), and solvent (DMF or DEF). Powder X-Ray diffraction (PXRD) patterns obtained were analyzed by the pattern matching MATLAB software. Acid modulators and reaction temperature were proven to be the major factors of synthesis under a fixed synthesis time (18 h) for each MOFs: MOF-525 (acetic acid and 90 °C), MOF-545 (dichloroacetic acid and 130 °C), and PCN-223 (acetic acid and 90 °C). Smaller particles were obtained after reducing the acid modulator amount, and the morphology shifted from MOF-525 to PCN-223 when the amount of the acid modulator was increased.

Morris et al. investigated the effect of modulators and the formation of defect sites [38]. Eighteen monocarboxylic acids of small aliphatic, aromatic, and long-chain kinds were tested, and the ratio of [modulator]/[TCPP] was varied from 10 to 6,000. Other synthesis conditions were fixed: substrate mixture of zirconium chloride (7 mg, 0.03 mmol) and TCPP (10 mg, 0.013 mmol) in DMF (10 mL). The reaction mixtures were then heated at 120 °C for 16 h. A pure phase MOF-525 was produced only with long-chain modulators (~38 mmol) of myristic (C_{14}) or stearic acid (C_{18}), and the synthesized MOF samples with weak acid modulators showed a high fraction of MOF-525. A pure PCN-222 was synthesized with small aliphatic modulators of difluoroacetic acid (~0.076 mmol) or formic acid (~76 mmol), and the synthesized samples with strong acid modulators showed a high fraction of PCN-222. An intermediate strong acid modulator, propionic acid (~76 mmol), produced PCN-223. While TCPP and modulator species with varying extent of deprotonation exist during the MOF formation process, only the fully deprotonated ligands and modulators can be directly coordinated to Zr clusters to form a specific Zr-based porphyrinic MOF structure. Consequently, the concentration ratio of fully deproton-

ated modulators and ligands ([Mod^-]/[$TCPP^{4-}$]) can serve as a useful guide for the MOF synthesis, as shown in Fig. 5. This value can be increased with higher acidity or concentration of the modulators. Thus PCN-222 is formed when the ratio of ([Mod^-]/[$TCPP^{4-}$]) is high so that a thermodynamically favored structure is expected, whereas MOF-525 is formed when the ratio is low so that a kinetically selected structure is expected.

MOF-525 with different particle sizes was synthesized by Liao et al. [41]. As the benzoic acid amount was decreased (from 2.7 to 0.9 g), the particle size of MOF-525 decreased (from 700 to 100 nm). MOF-525 produced with a small amount of benzoic acid (0.9 g) showed a distorted cube morphology, which may have been caused by insufficient crystallization due to the low concentration of benzoic acid, leading to faster crystallization of MOF-525. In the case of PCN-224, a size-controlled synthesis was attempted by controlling the amount of DMF (80 to 140 mL), benzoic acid (2.2 to 3.3 g), and TCPP (50 to 150 mg) [42]. The increased amount of benzoic acid resulted in bigger particles, whereas the amounts of DMF and TCPP showed the opposite trend. It was speculated that the low concentration of PCN-224 monomer formed under the increased benzoic acid produced the bigger particle size.

The effect of synthesis temperature on the crystal phase of Zr-based porphyrinic MOFs was investigated by Farha et al. [40]. A Zr_6 node solution with formic acid and a TCPP solution were prepared in DMF, respectively. Then, the Zr_6 node solution was heated at different temperatures from room temperature to 145 °C for 24 h, while the TCPP solution was added at a rate of 0.5 mL/min. At room temperature, a mixture of MOF-525 and PCN-224 was obtained. The product changed from MOF-525 and PCN-224 to PCN-222 when the synthesis temperature and time were increased to 145 °C and seven days. These results indicate that the synthesis of MOF-525 and PCN-224 having the parallel TCPP group in the structures is kinetically-controlled, whereas PCN-222 having the antiparallel TCPP group is thermodynamically-controlled.

Seed-mediated synthesis was explored by Zhou et al. [39], which led to pure phases of PCN-222, PCN-224(Ni), and PCN-225. A high purity targeted MOF structure could be prepared after introducing seed crystals. The introduction of seed crystals initiates a heterogeneous process, which is kinetically favored for the growth of targeted MOF structure and requires much lower driving force energy by skipping the nucleation stage involved in the homogeneous crystallization process.

Matute et al. reported a microwave-assisted synthesis of PCN-222 [43]. PCN-222 could be synthesized using two acid modulators (2-fluorobenzoic acid and trifluoroacetic acid) at 150 °C for 20 min under microwave-assisted conditions (35 W, 1 bar). Similarly, our group conducted a sonochemical synthesis of MOF-525 and MOF-545. The pure phase of both MOFs could be obtained within 2.5 and 0.5 h, respectively. The optimal synthesis conditions were investigated covering the variables of power (500 W full), time, pulse (5 sec (on)/3 sec (off)), and modulator, and high purity MOFs were synthesized for MOF-525 (power: 40%, 2.5 h, pulse, and benzoic acid) and MOF-545 (power: 60%, 0.5 h, no pulse, and trifluoroacetic acid).

An acid treatment on PCN-222 and NU-902 with 8 M HCl was required to remove the unreacted ligand and modulator trapped inside pores after the synthesis [44,45]. It was found that mesoporosity increased in PCN-222, and small mesoporosity was observed in NU-902 by removing a small fraction of the ligand leading to defect sites.

Mixed-ligand MOFs (MLMs, MLM-1 to 3) in **csq** topology were reported by Lee et al. [46]. These were built from Zr_6 clusters and the appropriate ratio of TCPP(Zn) and 1,3,6,8-tetrakis(*p*-benzoic acid)pyrene (TBAPy) ligands, both of which exhibited the same connectivity and similar size. Zr-based porphyrinic MOFs with two mixed-ligand (different connectivity) were also reported by Zhou et al. [47,48]. PCN-134 was in a 3D layer-pillar structure made of 2D layers composed of Zr_6 clusters and benzene tribenzoate (BTB), connected by TCPP between the 2D layers. Controlling the amount of the pillar linker TCPP led to structural defect sites during the synthesis of PCN-134. Similarly, PCN-138 in a face-sharing cuboctahedron structure was synthesized using 4,4′,4″-(2,4,6-trimethylbenzene-1,3,5-triyl)tribenzoate (TBTB) and TCPP based on Zr_6 clusters.

CHARACTERIZATION

Table 1 shows the typical synthesis conditions and key textural properties of the Zr-based porphyrinic MOFs reported. Generally, the successful synthesis of Zr-based porphyrinic MOFs can be confirmed by PXRD, scanning electron microscopy (SEM)/transmission electron microscopy (TEM), N_2 adsorption-desorption isotherms, and Fourier-transform infrared spectroscopy (FT-IR). Metalation can be confirmed by UV-Vis spectroscopy. Fig. 6 shows the simulated PXRD patterns of different Zr-based porphyrinic MOFs. MOF-525 and PCN-221 show the same patterns because of their same topology (**ftw**) (constructed from different Zr cluster units). The different morphologies of the Zr-based porphyrinic MOFs can be examined by SEM (Fig. 7), and uniform mesopore channels in MOF-545 were observed by TEM. From the N_2 adsorption-desorption isotherms, textural properties, including the surface area, pore volume, and pore size distribution, can be measured (Fig. 8); only MOF-545 shows a type IV isotherm and the rest of the Zr-based porphyrinic MOFs usually show type I isotherms

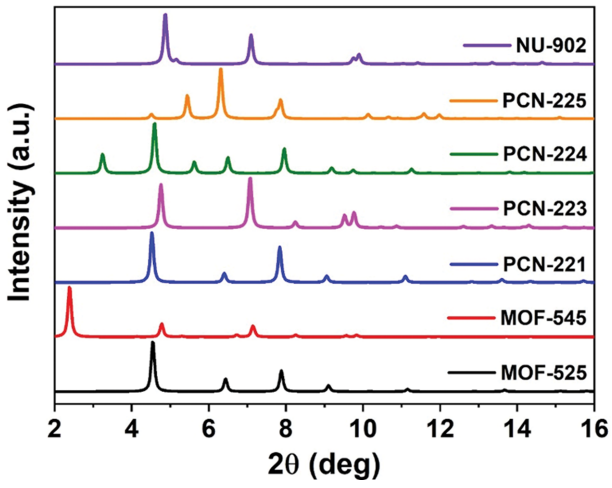

Fig. 6. PXRD patterns of Zr-based porphyrinic MOFs.

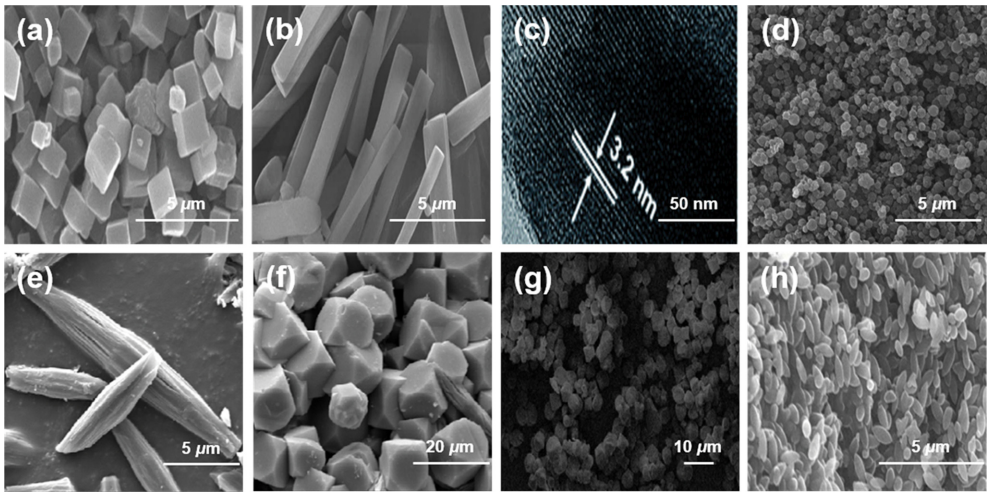

Fig. 7. SEM (TEM) images of Zr-based porphyrinic MOFs: (a) MOF-525, (b) MOF-545, (c) MOF-545 (TEM), (d) PCN-221, (e) PCN-223, (f) PCN-224, (g) PCN-225, and (h) NU-902. Modified from Ref. [39,45,51,54,55] with permission from copyright holders.

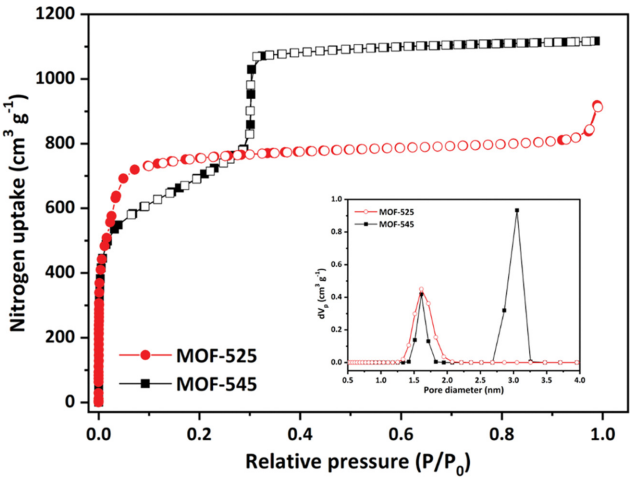

Fig. 8. N_2 adsorption-desorption isotherms of MOF-525 and MOF-545 (inset shows the corresponding pore size distributions). Adapted from Ref. [30] with permission from copyright holders.

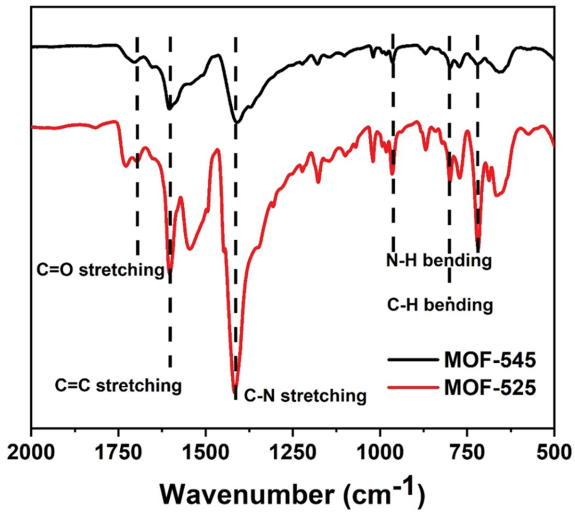

Fig. 9. FT-IR spectra of MOF-525 and MOF-545.

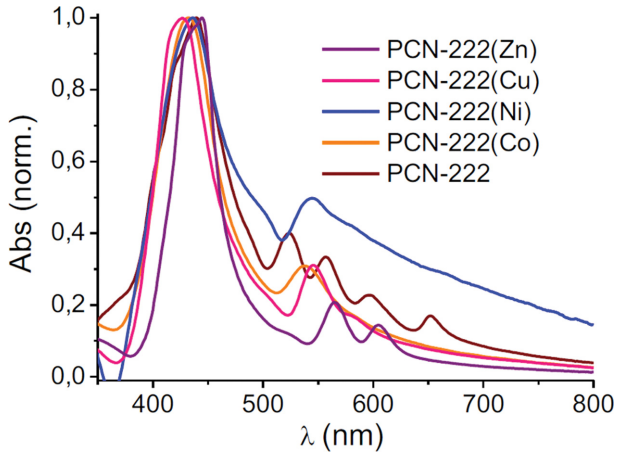

Fig. 10. Normalized UV-Vis spectra of PCN-222(M). Adapted from Ref. [43] with permission from copyright holders.

similar to the case of MOF-525 shown. FT-IR spectra of MOF-525 and MOF-545 exhibit the characteristic peaks, as given in Fig. 9. Because Zr-based porphyrinic MOFs can exist together in a product with different proportions, several characterization tools combined together (such as PXRD, N_2 adsorption-desorption isotherms, and SEM) will provide a more accurate assessment of the product quality. UV-vis is a simple method to confirm the progress of the MOF metalation. Fig. 10 shows the shifted Soret and Q-bands for the PCN-222 samples metallated with different elements.

During the synthesis of MOFs, vacancies of the linker or/and metal clusters can result to form crystal defect sites, leading to different physicochemical properties such as stability, surface area, gas adsorption behavior, and catalytic activity compared with the defect-free MOFs [56,57]. The defect sites in the Zr-based porphyrinic MOFs can be tuned by controlling the acidity (pK_a) and the amount of the modulator used, which produce Zr clusters terminated with the modulator instead of TCPP due to the stronger coordination by the acidic modulator with the Zr cluster [58,59].

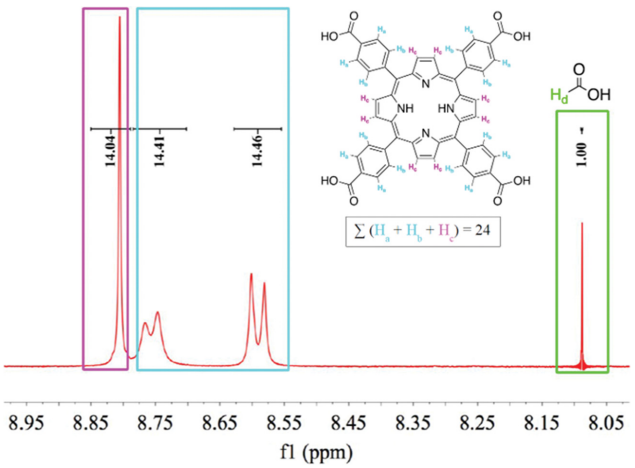

Fig. 11. ^{1}H NMR spectra of a digested FA-6000 (PCN-222) in deuterated dimethyl sulfoxide (DMSO). Adapted from Ref. [38] with permission from copyright holders.

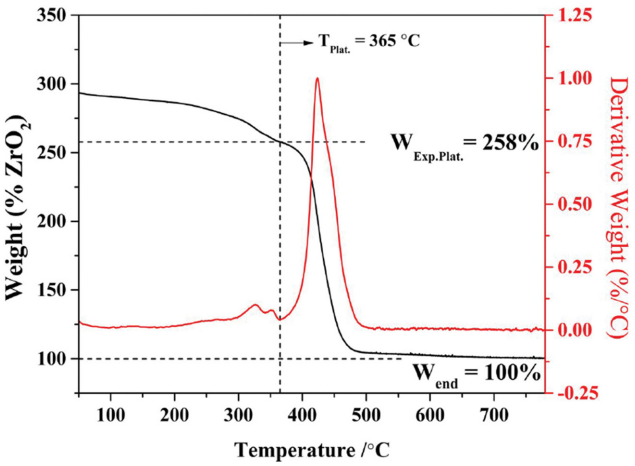

Fig. 12. TGA analysis of DFA-600 (PCN-222). Adapted from Ref. [38] with permission from copyright holders.

The number of defect sites can be estimated by ^{1}H nuclear magnetic resonance (NMR), thermal gravimetric analysis (TGA), and inductively coupled plasma mass spectrometry (ICP-MS) [38]. The amount of deficient linker can be calculated using the ratio of [modulator]/[TCPP] from ^{1}H NMR and amount of zirconium oxide (ZrO_2) residue from TGA as shown in Figs. 11 and 12, when compared against the ideal molecular formula of the Zr-based porphyrinic MOFs [38]. This method may have some limitations, such as the error caused by the potential presence of other MOF species, modulator trapped inside pores, and the underestimated modulator after acid treatment for measuring the ratio [modulator]/[TCPP] by ^{1}H NMR. In the case of the deficient Zr clusters, the amount of Zr estimated from the digested Zr-based porphyrinic MOFs by ICP-MS can provide information on the vacancy in Zr clusters when compared with the theoretical Zr concentration in the MOF. The information on the surface area and pore size distribution can also give a rough estimate of the comparable defect sites in different MOF samples, despite their limitation to quantify the defect sites in the MOF products. Usually, higher surface area with wider pores is expected for the MOF sample with more defect sites [60].

FUNCTIONALIZATION

Specific functionalization of MOFs is necessary to generate active sites for adsorption and catalysis [14,61]. Zr-based porphyrinic MOFs have 1) a built-in functionality from TCPP, with which various transition metal ions can be immobilized via coordination bonding, 2) grafting for an organic or organometallic species is possible onto the coordination-unsaturated Zr or metalloporphyrin sites, 3) a simple impregnation of metal ions followed by a suitable reduction process produces metal nanoparticles, and 4) a composite with fiber or core-shell structure can be prepared. Applying the MOF as a sacrificial template to generate a metal supported on an N-doped carbon or N-doped carbon after removing the metal oxide is also receiving growing attention.

1. Metalation

Various metal sources have been reported for metalation on Zr-based porphyrinic MOFs (see Table 1). The porphyrin ligand in the Zr-based porphyrinic MOFs can be metallated via a pre- or post-synthesis procedure in the presence of an excess amount of metal source. The former involves MOF synthesis using a pre-metallated ligand, TCPP(M), and the latter consists of the introduction of the metal source after the MOF synthesis. Zr^{4+} is known not metallated on porphyrin ligands during the synthesis of Zr-based porphyrininc MOFs [16]. Pre-metalation seems more precise to introduce a known amount of a specific metal ion to a porphyrinic MOF. Still, a separate synthesis step for TCPP(M) preparation is demanded. An unusual double metalation was also reported, in which Fe^{3+} ions were metallated on the Zr cluster of PCN-222(Fe) using anhydrous $FeCl_3$ [62]. A similar metalation process on MOF-808 was reported [63]. UV-vis spectroscopy is useful for checking metalation.

2. Grafting

The unsaturated Zr sites in Zr-based porphyrinic MOFs can often be utilized for grafting of an organic/organometallic species. MOF-545(M), comprised of mesopores in high stability, has often been functionalized by grafting. Organic molecules having carboxylate or phosphonate functional groups were immobilized via interaction with Zr clusters by coordination bonding [64,65]. 1-Methyl-3-(2-carboxyethyl)imidazolium bromide (ImBr) ionic liquid was grafted on MOF-545(Mn) [66], and the different perfluoroalkyl acids were grafted on PCN-222(Fe) to increase the hydrophobicity of the material, as shown in Fig. 13(a) [24].

The metalloporphyrin ligand in the MOF can also be used as a platform for grafting. A biomimetic organometallic $[Fe_2S_2]$ complex $[(\acute{\imath}\text{-}SCH_2)_2NC(O)C_5H_4N]\text{-}[Fe_2(CO)_6]$ was post-synthetically grafted on the metallated Zn sites of MOF-545(Zn), as shown in Fig. 13(b) [67].

3. Metal Impregnation

Controlling the size and stability of nanoparticles is vital for improving the catalytic activity against the tendency of easy self-aggregation [68]. To this end, nanoporous materials are often used to support metal nanoparticles.

Three Zr-based MOFs, UiO-66, NU-902, and PCN-222, having

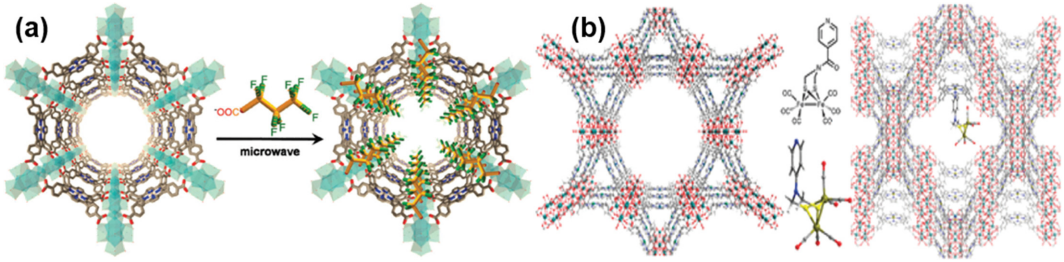

Fig. 13. Structure of (a) PCN-222(Fe)-F$_n$ and (b) [FeFe]@MOF-545(Zn). Adapted from Ref. [24,67] with permission from copyright holders.

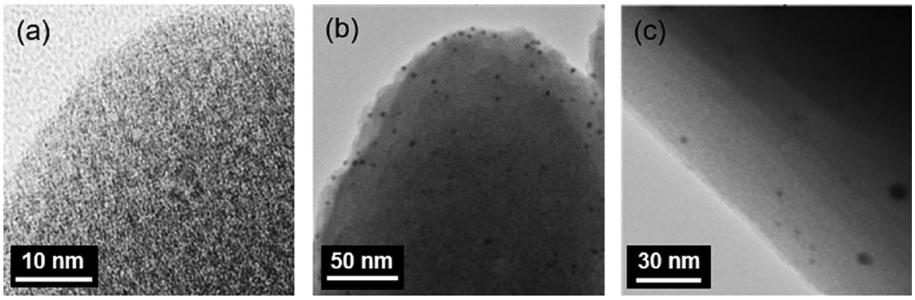

Fig. 14. TEM images of (a) Pd@UiO-66, (b) Pd@NU-902, and (c) Pd@PCN-222. Adapted from Ref. [69] with permission from copyright holders.

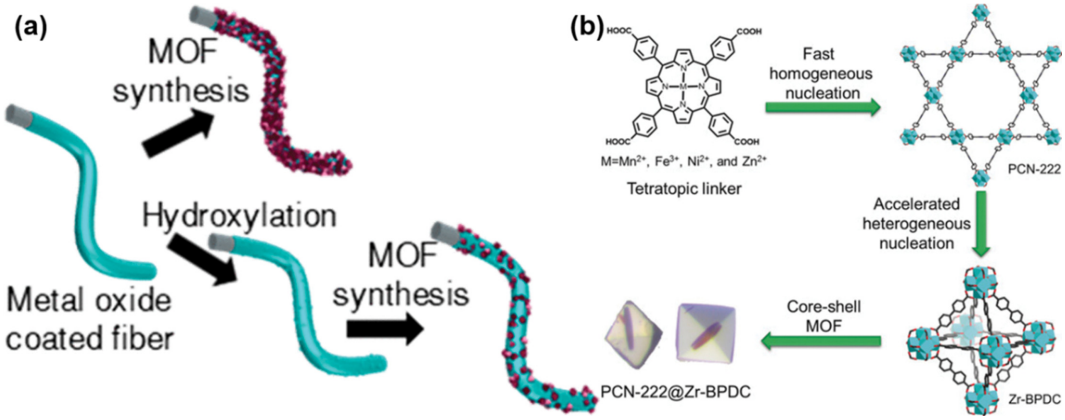

Fig. 15. Synthesis of (a) MOF-525-fiber and (b) core-shell PCN-222 composites. Adapted from Ref. [73,74] with permission from copyright holders.

different pore sizes and topologies, were tested to impregnate Pd nanoparticles. Different average Pd nanoparticle sizes were obtained: Pd@UiO-66 (1.3 nm), Pd@NU-902 (2.2 nm), and Pd@PCN-222 (3.4 nm) as shown in Fig. 14, which indicated that pore size of the MOFs (UiO-66: ca. 1.2 nm, NU-902: ca. 1.2 and 3.0 nm, and PCN-222: ca. 1.2 and 3.2 nm) affected the nanoparticle growth during the impregnation procedure [69]. Pt nanoparticle impregnation was also attempted on PCN-224(M) (M: Zn, Ni, Co, Mn, or 2H), and the concentration of the added polyvinylpyrrolidone (PVP, MW=55,000) was a pivotal factor in adjusting the average particle size during the impregnation [70]. The average particle size obtained with $H_2PtCl_6 \cdot H_2O$ on PCN-224(M) was ~2.5 nm (1.125 M of PVP), ~10 nm (0.375 M of PVP), and ~14 nm (without PVP), respectively. PCN-224(Cu)/TiO_2 was obtained by impregnation of TiO_2 during the synthesis of PCN-224(Cu), which produced well-dispersed TiO_2 particles because of the uniform pore size of porous PCN-224(Cu) [71].

4. Composite

MOF composites can provide multifunctionality, new property, or new applicability, which cannot be achieved by a single MOF component [72].

A composite of MOF-525 crystals attached to metal oxide-coated polypropylene (PP) fiber was prepared, as shown in Fig. 15(a) [73]. These MOF composites draw attention because of their potential for the capture or degradation of chemical warfare agents [75,76]. A metal oxide (Al_2O_3, TiO_2, ZnO, HfO_2, or ZrO_2) was coated on PP fiber by atomic layer deposition (ALD). Hydroxylation of the metal oxide layer was confirmed to be a critical factor for MOF nucleation on them. A small amount of water present in the MOF synthesis, such as from the metal salt, was sufficient to trigger hy-

droxylation, which induces MOF adsorption and subsequent nucleation. However, a high extent of hydroxylation with physisorbed water was undesirable, slowing down the MOF growth.

MOF-525 grown on graphene nanoribbons (GNRs) was also prepared through a one-step synthesis [77]. A small amount of GNRs was added during the synthesis of MOF-525 to induce the in-situ growth of the MOF crystals on GNR. The products showed highly dispersed MOF-525 crystals due to C-O functional groups of GNRs surface, which promoted the nucleation of MOF-525 and prevented the aggregation of GNRs. The nanocomposite could also be fabricated as a film for electrochemical applications.

One-pot synthesis of PCN-224(M) (M: Ni, Co, Ru, or 2H) inside a melamine foam (MF) was also reported [78]. It was prepared by conducting solvothermal synthesis of the MOF using a metallated TCPP, zirconium chloride, and benzoic acid over an acid-treated MF for three days at 120 °C. The enhanced catalytic properties of PCN-224(M)/MF were explained by the hierarchical pore structure, improving the diffusion of the substrate to the active sites.

A novel Zr-based core-shell MOF composite of PCN-222@Zr-BPDC (UiO-67) was prepared using a single zirconium source with two different ligands of TCPP and biphenyl-4,4′-dicarboxylate (BPDC) by controlling the nucleation kinetics as shown in Fig. 15(b) [74]. TCPP binds with the metal cation fast, forming PCN-222 via homogeneous nucleation, which acted as a seed for heterogeneous nucleation of the UiO-67 shell. Both metalation of the PCN-222 and isoreticular expansion of the shell by changing the length of the ligand were demonstrated.

5. Pyrolysis

MOFs can be used as useful precursors for porous carbons via pyrolysis under Ar or N_2 gas flow conditions. They are mostly tested as electrocatalysts or supercapacitors, and the status of their current development was reported in several review articles [8,79,80]. Also, single-atom catalysts (SACs) derived from MOF pyrolysis draw great attention due to the high catalytic efficiency from the coordinatively unsaturated metal atom sites [81-83]. Depending on the treatment conditions of the pyrolysis temperature, treatment time, and gas flow conditions, porous carbons with different physicochemical properties are obtained [84]. Zn in a ZIF-8/67 on cellulose nanofibers composite, for example, vaporize above 700 °C in the process and creates pores upon its release, producing a carbon with high surface area and mesopores with well-distributed CoOx, which is effective for oxygen reduction reaction (ORR) [85]. Frequently, nitrogen species in the MOF's organic constituents or introduced by impregnation using a suitable chemical are retained after pyrolysis to produce an N-doped carbon, the amount of which is also affected by the pyrolysis conditions. Therefore, an optimization of the pyrolysis condition is essential to obtain the desired carbon product.

Nanoporous carbons (NCs) derived from MOF-525 were prepared from MOF-525 with different particle sizes (obtained by controlling the modulator amount) via pyrolysis under N_2 atmosphere [87]. The carbon material obtained was treated with 10 wt% of HF solution to remove zirconia, and the final product was used as a supercapacitor.

A single-atom (SA) Fe-implanted N-doped porous carbon (Fe_{SA}-N-C: 1.76 wt% of Fe) was prepared from pyrolysis of Fe_{20}-PCN-222 followed by HF (20 wt%) washing to remove zirconia [55]. The Fe_x-PCN-222 (x=Fe-TCPP amount) was synthesized using a mixture of TCPP and Fe-TCPP ligands in different proportions to obtain SAC, since enough distance was necessary between the Fe

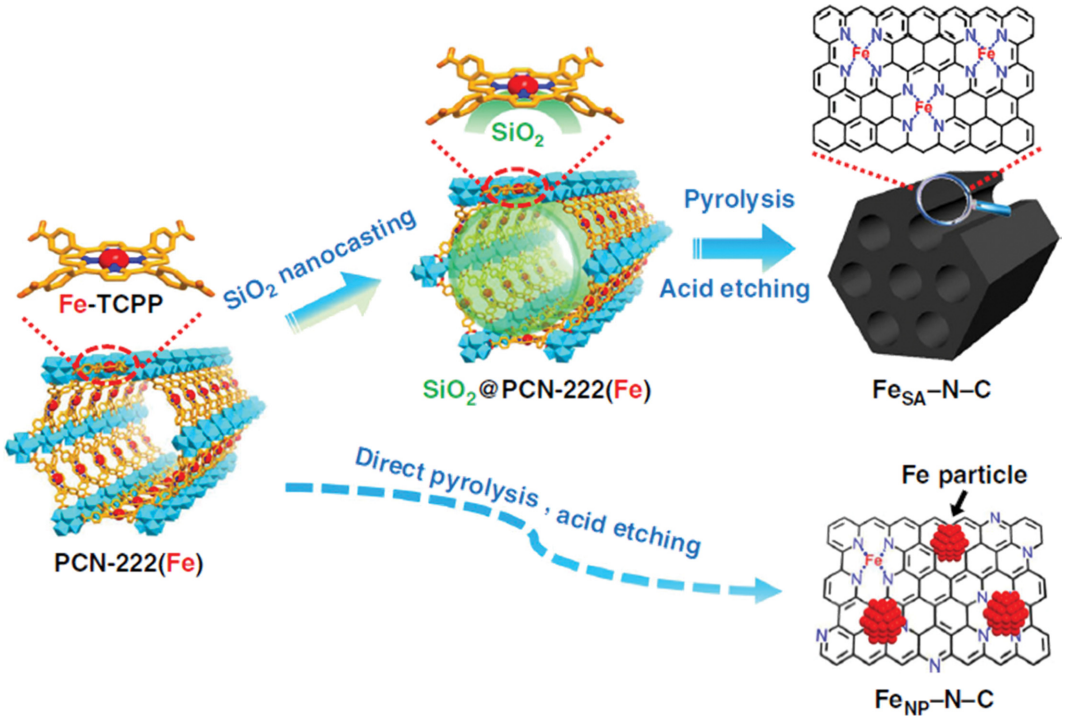

Fig. 16. Schematic illustration of Fe_{SA}-N-C from SiO_2@PCN-222(Fe). Adapted from Ref. [86] with permission from copyright holders.

atoms to inhibit the agglomeration during the pyrolysis. An alternative synthetic strategy for a SAC was proposed by introducing SiO_2 casts inside the mesopore of PCN-222(Fe) to prevent agglomeration, as shown in Fig. 16 [86]. SiO_2 casts were formed by mixing PCN-222(Fe) and tetraethylorthosilicate (TEOS). The Fe_{SA}-N-C from SiO_2@PCN-222(Fe) could achieve high-loading of Fe SA sites (3.46 wt%). The hierarchical porosity and Fe SA sites in Fe_{SA}-N-C could facilitate the high accessibility to the active sites by enhanced mass transfer in electrochemical reactions [88].

ADSORPTION APPLICATIONS

One of the most efficient methods for removing hazardous organic/inorganic moieties from wastewater, air, or fuel is adsorptive separation employing a porous material. It is simple to operate, low cost, and produces no harmful by-products. Zr-based porphyrinic MOFs are increasingly investigated as an adsorbent utilizing the porphyrin units' unique chemical properties incorporated into the water-stable MOF structures (see Table 2).

1. Aqueous Organic Pollutants

Organic dyes are toxic and carcinogenic pollutants, mostly generated by the textile industry. Li et al. reported that PCN-222 adsorbed 906 mg/g of anionic methylene blue (MB) and 589 mg/g of cationic methyl orange (MO) in an aqueous solution [89]. PCN-222 had an isoelectric point at pH 8 with the potentials of 23.5 and −13.6 mV in the range of pH 3-10. Accordingly, electrostatic interaction was responsible for capturing both anionic and cationic dyes under appropriate pH conditions. A mutual enhancement (36.8% for MB and 73.5% for MO) in the adsorbed amounts was also observed in a mixed dye sample, which was explained by a push-pull mechanism in that the self-assembled dye dimers formed by π-π interaction between the monomers attracting the counter-charged dye species, and the combined dye species were adsorbed on the PCN-222 surface. Recently, a metallated PCN-222(Fe) was also applied for adsorption of dyes and compared with the commercial activated carbon (AC) [90]. PCN-222(Fe) showed far superior adsorption of the large anionic and cationic dyes to AC: brilliant green (BG: 854 mg/g), crystal violet (CV: 812 mg/g), acid red 1 (AR 1: 417 mg/g), and acid blue 80 (AB 80: 371 mg/g), which was explained by the mesoporous nature of PCN-222(Fe) combined with electrostatic and π-π interactions. On the other hand, the adsorption of small-sized dyes (MB and MO) showed not much difference between PCN-222(Fe) and AC.

Bisphenol A (BPA) is one of the most common endocrine-disrupting chemicals (EDCs). BPA was efficiently adsorbed (maximum adsorption of 487 mg/g) and subsequently photodegraded by PCN-222 [91].

The antibiotic drug sulfamethoxazole (SMX), broadly used to treat bacterial diseases, introduces toxicity into the aquatic environment. It was efficiently adsorbed by MOF-525 and MOF-545, respectively: MOF-545 with the adsorption amount of 690 mg/g and MOF-525 with 585 mg/g [30]. The mesopore structure in MOF-545 and high surface area enabled the high adsorption equilibrium capacity and fast kinetics (<30 min). The porphyrin units in the structure were effective for adsorption via π-π interaction and H-bonding with the SMX molecules. The adsorption/desorption cycles were repeated four times without significant deterioration after acetone washing, and the stability of the MOF-545 was

Table 2. Adsorption and separation studies carried out over Zr-based porphyrinic MOFs

MOFs	Target components	Comments	Ref.
PCN-222	Methylene blue (MB), Methyl orange (MO)	• High and fast adsorptive removal of various anionic and cationic dye species. • Mutually enhanced adsorption in a mixed dye solution (push-pull mechanism).	[89]
PCN-222(Fe)	Brilliant green (BG), Crystal violet (CV), Acid red 1 (AR 1), Acid blue 80 (AB 80)	• High adsorption for big dyes by electrostatic, π-π interaction, and van der waals forces (mesopores). • No significant differences in adsorption between PCN-222(Fe) and activated carbon for small dyes (MB, MO).	[90]
PCN-222	Bisphenol A (BPA)	• High adsorption of BPA followed by photodegradation under visible light. • BPA oxidized by the singlet oxygen ($^1O_2$) generated from porphyrin ligand.	[91]
MOF-525, MOF-545	Sulfamethoxazole (SMX)	• High adsorption of SMX by π-π interaction, H-bonding, and high surface area. • Mesoporosity in MOF-545 exhibited faster adsorption than MOF-525.	[30]
PCN-222	CO_2, CH_4, N_2	• Selectively separating CO_2/N_2 and CO_2/CH_4.	[96]
PCN-X-X% Fe or Al	CO_2	• Metalation effect on CO_2 adsorption. • Al^{3+} exhibited a higher enhancement than Fe^{3+}.	[97]
PCN-224	CH_4, C_2H_6, C_3H_8	• Selectively adsorption and separation of C_2H_6 and C_3H_8 from CH_4.	[98]
PCN-223, NU-902, PCN-222, MOF-525	Ethanol	• Adsorption isotherms of ethanol at 298 and 353 K. • Estimation of working capacities for refrigeration and ice-making system.	[99]
PCN-224	2,4,6-trinitrotoluene (TNT)	• Fluorescent detection sensor for TNT in water.	[29]
NU-902	Cd^{2+}	• Fluorescent detection within 2 min for an aqueous Cd^{2+} solution (0.3 ppb). • Immobilized on a PVC membrane.	[100]
PCN-221	Hg^{2+}	• Fluorescent detection sensor for Hg^{2+} ions. • Hg^{2+} adsorption: pseudo-second order kinetics; 95% removal (50 ppm) in 30 min.	[54]

confirmed by PXRD and FT-IR.

2. CO_2, C_2/C_3 and Ethanol in Gas Phase

CO_2 capture via adsorption is an active research topic for alleviating the global warming problem [92]. Among the various adsorbent materials, MOFs are emerging as a useful candidate, and the status of the materials synthesis, functionalization, and CO_2 capture performances are discussed in several recent review articles [93,94]. MOFs incorporated with N- donors and open metal sites usually show high CO_2 adsorption and relatively high heat of adsorption [95].

PCN-222 was tested for adsorptive separation CO_2/CH_4 and CO_2/N_2 by adsorption isotherms and breakthrough experiments [96]. CO_2 adsorption amount was 1.16 mmol/g (at 100 kPa) and 13.67 mmol/g (at 3,000 kPa) at 298 K, and the adsorption selectivity was 4.3 (CO_2/CH_4 (50 : 50, v/v)) and 73.7 (CO_2/N_2 (50 : 50, v/v)), respectively, at 298 K and 100 kPa. Relatively low isosteric heat of adsorption (18.3 KJ/mol) was estimated, and the CO_2 adsorbed could be completely desorbed in 10 min under a He flow of 40 mL/min. When compared with other MOFs, PCN-222 showed only a moderate amount of CO_2 adsorption at low pressure condition. Amine-functionalization on PCN-222 is an option to increase the CO_2 capture capacity. Alternatively, open metal Lewis acidic sites were created by metalation to Zr-based porphyrinic MOFs, designated as PCN-X (a mixture of PCN-223 and MOF-525) to enhance the CO_2 adsorption [97].

PCN-224 was tested for separating C_2H_6 and C_3H_8 from CH_4 for separation of light hydrocarbons in natural gas [98]. At 298 K, the adsorption capacities of C_2H_6 (2.94 mmol/g) and C_3H_8 (8.25 mmol/g) were much higher than CH_4 (0.47 mmol/g) at 100 kPa. In addition, the calculated selectivity values by the ideal adsorbed solution theory (IAST) were moderately high: 12 for C_2H_6/CH_4 and 609 for C_3H_8/CH_4, respectively. The breakthrough experiment also exhibited efficient dynamic separation in the C_2/C_1 and C_3/C_1 mixtures.

For the performance evaluation of the adsorption cooling system utilizing the Zr-based porphyrinic MOFs and ethanol pair, the adsorption isotherms of ethanol were measured over PCN-223, NU-902, PCN-222, and MOF-525 having different topology and pore size at 298 and 353 K [99]. Based on the adsorption isotherms of ethanol, the working capacity for refrigeration and ice-making was calculated by the differences in the adsorbed ethanol amounts at the adsorption (268 K and 278 K, respectively) and the desorption conditions (353 K). MOF-525 was the most efficient adsorbent for ethanol in the both cases. The optimum MOF pore size for ice-making, refrigeration, and heat pump using ethanol was estimated to be ca. 1.5, 2, and 3-4 nm, respectively.

3. Fluorescence Detection of Hazardous Species in an Aqueous System

Porphyrins show fluorescence, and upon complexation with various organic/inorganic guest species the fluorescence is progressively quenched in correlation with the guest concentration. On the other hand, porphyrins tend to strongly aggregate in aqueous solution due to the strong π-π interaction, and cause diminishing fluorescence response to the analyte. Thus, porphyrin has often been immobilized on a suitable heterogeneous carrier. In this regard, Zr-based porphyrinic MOFs with porphyrin as an inherent organic constituent in isolation over a strongly water-stable framework are promising as a fluorescent detection sensor.

2,4,6-Trinitrotoluene (TNT) is a commonly used explosive and highly toxic, and its accurate detection is important for both environment and national security. PCN-224 was reported excellent for the fluorescent detection of TNT in water with rapid response time (30 sec) and the detection limit of 0.46 μM [29]. TNT forms a complex with the porphyrin units in PCN-224 via hydrogen bonding and π-π stacking, which quenches the fluorescence emission from PCN-224 progressively, depending on the TNT concentration. Similarly, NU-902 in powder form was tested for the detection of Cd^{2+} ions, and the fluorescence quenching was observed in the Cd^{2+} level as low as 0.3 ppb [100]. A MOF composite with polyvinylchloride (PVC) was also fabricated, and the fluorescence quenching was observed after 5 to 60 min for a 0.1 M Cd^{2+} solution. PCN-221 was also reported for detecting Hg^{2+} ions with the fluorescent response time under 1 min and the detection limit of 0.01 μM [54]. They also measured the Hg^{2+} adsorption capacity of 234 mg/g, and equilibrium was reached within 30 min in water solution. The interaction between Hg^{2+} ions and N Lewis base sites in the porphyrin ligand was confirmed by UV-Vis spectroscopy.

CATALYTIC APPLICATIONS (I): HETEROGENEOUS CATALYSIS

Zr-based porphyrinic MOFs have been increasingly applied as a heterogeneous catalyst for chemical conversions, photocatalysis, and electrocatalysis as listed in Table 3.

1. Epoxidation

MOF-525(Mn) was applied for epoxidation of styrene in the presence of isobutyraldehyde (IBA) and O_2 flow (30 cm^3/min) at room temperature (Scheme 1), and its catalytic activity was compared with the TCPP-Mn homogeneous catalyst [27]. Styrene conversion of 99% with a styrene oxide yield of 83% was obtained after 2.5 h reaction. The measured activation energy was ca. 43 kJ/mol. PCN-222(Fe)@UiO-67 core-shell structure was tested for epoxidation of olefins using iodosobenzene (PhIO) as an oxidant at room temperature [74]. As the olefin size increased, the olefin conversion decreased despite longer reaction time due to the microporous outer shell of UiO-67, which blocked the catalytic sites located in the inner shell of PCN-222(Fe). Hierarchical MOF/MF composites having meso- and macropores were prepared using different metallated PCN-224 (metal: Fe, Ni, Co, or Ru) in varying loading amounts (MF: 50, 100, 150, 200, and 350%) and applied for the epoxidation of cholesteryl esters [78]. For the epoxidation of cholesteryl acetate, PCN-224$(Ru)_{200\%}$/MF (PCN-224 size of 600 nm) showed the highest yield (92%) in the presence of 2,6-dichloropyridine N-oxide (Cl_2pyNO) as an oxidant at room temperature after 30 h. The product yield by other composite materials, PCN-224$(Fe)_{200\%}$/MF (34%) and PCN-224$(Co)_{200\%}$/MF (41%), was lower even after longer

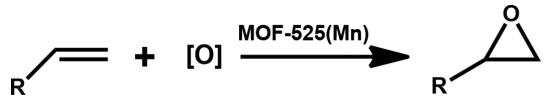

Scheme 1. Epoxidation of olefins.

Table 3. Heterogeneous catalysis studies carried out over Zr-based porphyrinic MOFs

Catalytic reaction	Sample	Reaction conditions			Other experimental details	Ref.
		Temp. (°C)	Time	Yield/performance		
Epoxidation	MOF-525(Mn)	R.T.	2.5 h	83%	Substrate: styrene/Oxidant: isobutyraldehyde (IBA)/O_2 (30 sccm)	[27]
	PCN-222(Fe)@Zr-BPDC(UiO-67)	R.T.	12, 24 h	41-99%	Substrate: alkenes/Oxidant: PhIO	[74]
	PCN-224(Ru)200%/MF	R.T.	36 h	92%	Substrate: cholesteryl esters/Oxidant: Cl_2pyNO	[78]
CO_2 cycloaddition	PCN-224(Co)	100	4 h	42%	Substrate: propylene oxide/Co-catalyst: tetrabutylammonium chloride (TBACl)/CO_2 (2 MPa)	[52]
	PCN-222(Co)	R.T.	12 h	99%	Substrate: 1,2-epoxypentane/Co-catalyst: tetrabutylammonium bromide (TBABr)/CO_2 (1 atm)	[43]
Oxidative carboxylation	MCEIBr-MOF-545(Mn)	60	10 h	95%	Substrate: styrene/Oxidant: IBA/CO_2/O_2 (5/5 bar)	[66]
Oxidation	MMPF-6	-	-	4.34×10^{-4} mM/s 7.56×10^{-5} mM/s	Substrate: 1,2,3-trihydroxybenzene, 2,2′-azinodi(3-ethylbenzothiazoline)-6-sulfonate/Oxidant: H_2O_2/Solvent: ethanol	[101]
	PCN-222(Fe)	-	-	4.85×10^4, 8.59×10^3, 8.18×10^2 k_{cat}/K_m (M^{-1} min^{-1})	Substrate: pyrogallol, 3,3,5,5 tetramethylbenzidine, o-phenylenediamine/Oxidant: H_2O_2	[44]
	PCN-221(Fe)	65	11 h	87 and 5.4%	Substrate: cyclohexane/Oxidant: TBHP	[50]
	PCN-222(Fe)-F_7	80	24 h	46%	Substrate: cyclohexane/Oxidant: TBHP/Additive: $AgBF_4$/O_2 (1 bar)	[24]
Hydroxylation	MOF-525 on TiO_2/PP	-	20, 70 min	100%	Substrate: dimethyl-4-nitrophenyl phosphate (DMNP), 2-chloroethyl ethyl sulfide (2-CEES)	[73]
Dehydrogenation	Pd@NU-902, Pd@PCN-222	150	-	H_2: 3.6 and 3.3 mmol $(g\ Pd)^{-1}min^{-1}$	Substrate: methanol	[69]
O-H insertion	Ir-PMOF-1(Zr)	R.T.	10 min	94%	Substrate: isopropanol (^{i}PrOH), ethyl diazoacetate (EDA)	[103]
Hetero-Diels-Alder	PCN-223(Fe)	80	12 h	99%	Substrate: benzaldehyde with 2,3-dimethyl-1,3-butadiene/Additive: $AgBF_4$	[51]
Photocatalytic CO_2 reduction	PCN-222	R.T.	10 h	$HCOO^-$: 30 μmol	Conditions: 420-800 nm wavelength/acetonitrile and triehanolamine (TEOA) solution (60 mL, v/v: 10/1)	[110]
	MOF-525 (M: Co or Zn)	R.T.	6 h	CO: 200.6 μmol g^{-1} h^{-1} (MOF-525(Co)), 111.7 μmol g^{-1} h^{-1} (MOF-525(Zn)	Conditions: 400-800 nm wavelength/acetonitrile and TEOA solution (2 mL, v/v: 4/1)	[111]
	PCN-224(Cu)/TiO_2	R.T.	8 h	CO: 37.21 μmol g^{-1} h^{-1}	Conditions: ≥300 nm wavelength/D.I. water (2 mL)	[71]

reaction time (72 h). Steady catalytic activity of PCN-224$(Ru)_{200\%}$/MF was maintained even after the sixth reuse. Macropores in MOF and the well-dispersed PCN-222(Ru) contributed toward the enhanced diffusion and improved catalytic performance.

2. CO_2 Cycloaddition

CO_2 cycloaddition of propylene oxide was conducted under

Table 3. Continued

Catalytic reaction	Sample	Reaction conditions			Other experimental details	Ref.
		Temp. (°C)	Time	Yield/performance		
Photocatalytic oxidation and degradation	PCN-222	25	20 min	0.004 mg/min	Conditions: visible light intensity 109.2 mW/cm^2 Xe lamp (λ: from 400 to 700 nm) Substrate: bisphenol A	[91]
	PCN-222	R.T.	0.5 h	Blue LED $t_{1/2}$(CEES)=13 min	Conditions: white, red, or blue LED/ methanol solution (1 mL)/Oxidant: O_2	[114]
	Nanosize PCN-222	R.T.	1.5 h	$t_{1/2}$(DMNP)=8 min $t_{1/2}$(CEES)=10 min	Conditions: blue LED/methanol and 0.4 M *N*-ethylmorpholine solution (1 mL, v/v: 1/1)/Oxidant: O_2	[115]
	Pt/PCN-224(Zn)	R.T.	50 min	>99%	Conditions: visible light 100 mW/cm^2 (λ>400 nm)/Oxidant: O_2/Substrate: benzyl alcohol	[70]
	PCN-222	R.T.	45 min	100%	Conditions: 100 mW/cm^2 Xe lamp (λ>420 nm)/Oxidant: O_2/Substrate: benzylamine	[116]
	Fe@PCN-224	R.T.	1 h	Acetone: 280.7 ppm	Conditions: visible light 300 W Xe lamp with a cut-off filter (i.e., λ>400 nm, 21A)/Air/Substrate: isopropyl alcohol (IPA)	[117]
	Fe@PCN-222(Fe)	R.T.	32 h	79%	Conditions: LED light/acetonitrile and water solution (4 : 1 v/v)/O_2/Substrate: benzyl alcohol and 2-aminobenzamide	[62]
Photocatalytic H_2 generation	[FeFe]@MOF-545(Zn)	R.T.	2 h	3.5 mmol	Conditions: ≥420 nm wavelength/pH 5 D.I. water (1.0 M acetate buffer solution) and 20 mM ascorbic acid	[67]
Electrochemical reduction of CO_2	MOF-525(Fe)	-	>4 h	CO_2 and H_2: 15.3 and 14.9 μmol/cm^2	Conditions: 1 M $TBAPF_6$ acetonitrile electrolyte solution/additive: trifluoroethanol (TEE)	[28]
Electrochemical nitrite oxidation	MOF-525 film	R.T.	-	$\Delta J_{p,\ 0.75\ mM}$: 293.9 μAcm^{-2}	Sensitivity: 40.6 $\mu AmM^{-1}cm^{-2}$/Linear range: 10-800 μM/Limit of detection: 0.72 μM	[41]
	MOF-GNRs	-	-	$\Delta J_{p,\ 0.75\ mM}$: ca. 250 μAcm^{-2}	Sensitivity: 93.8 $\mu AmM^{-1}cm^{-2}$/Linear range: 100-2,500 μM, Limit of detection: 0.75 μM	[77]
Oxygen reduction reaction (ORR)	Fe_{SA}-N-C	-	-	J_k: 23.27 $mAcm^{-2}$	At 0.85 V in 0.1 M KOH	[88]
	Fe_{SA}-N-C (SiO_2 casted)	-	-	J_k: 37.19 $mAcm^{-2}$	At 0.85 V in 0.1 M KOH	[86]
Nitrogen reduction reaction (NRR)	Fe_1-N-C	-	-	NH_3: 1.56×10^{-11} $molcm^{-2}s^{-1}$	At −0.05 V vs. RHE and Faradaic efficiency of 4.51%	[55]

CO_2 (2 MPa) at 100 °C in the presence of tetrabutylammonium chloride (TBACl) as a co-catalyst over PCN-224(Co) [52]. PCN-224(Co) showed similar catalytic activity to the homogeneous cobalt porphyrin catalyst, and 42% conversion of propylene oxide was achieved after 4 h. No significant loss of catalytic activity was observed during the three recycle runs. PCN-222 and PCN-222(M) (M=Co, Ni, Cu, or Zn) were applied for the cycloaddition of

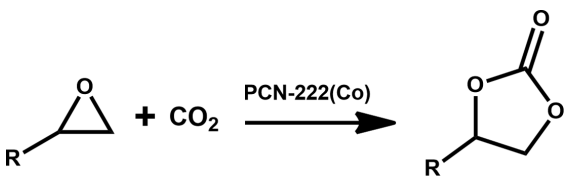

Scheme 2. CO_2 cycloaddition of epoxides.

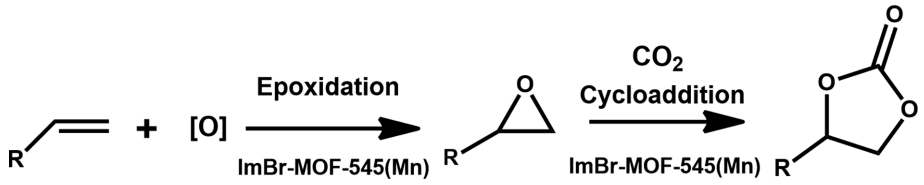

Scheme 3. Oxidative carboxylation of olefins.

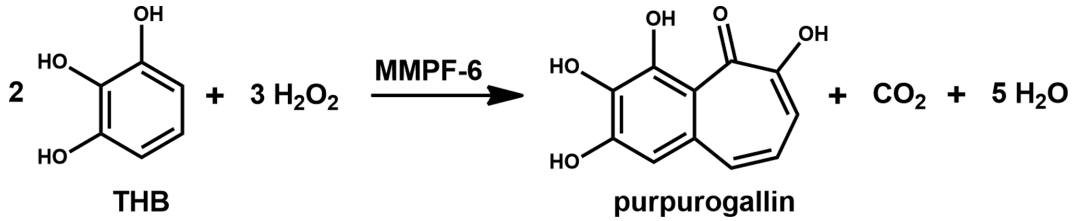

Scheme 4. Oxidation of 1,2,3-trihydroxybenzene (THB).

epoxides and azidirines with CO_2 (Scheme 2) [43]. MOF synthesis and metalation were carried out by microwave heating with a short synthesis time. The catalytic reactions were performed under CO_2 (1 atm) and at room temperature for 12 h (yield: 99%, substrate: 1,2-epoxypentane) and 27 h (yield: 73%, substrate: 1,2-epoxydecane) with tetrabutylammonium bromide (TBABr) co-catalyst. PCN-222(Co) showed the highest catalytic activity, followed by PCN-222(Zn)>PCN-222(Cu)>PCN-222(Ni). Also, the recyclability of PCN-222(Co) was established during the four recycles.

3. Oxidative Carboxylation

The post-synthesis-metallated MOF-545(Mn) was grafted with an imidazolium bromide ionic liquid, and the product, ImBr-MOF-545(Mn), was applied for the catalytic oxidative CO_2 cycloaddition reaction of styrene (Scheme 3) [66]. The one-pot cascade epoxidation-cycloaddition reaction is attractive due to the low-cost olefin starting chemical, no need to separate toxic epoxide intermediates, and minimized solvent usage. The cascade reaction was performed under mild conditions CO_2 (5 bar), O_2 (5 bar), solvent-free, and 60 °C for 10 h in the presence of IBA, which showed 99% of styrene conversion and 95% of styrene carbonate selectivity with no significant loss of catalytic activity during five recycle runs.

4. Oxidation

MMPF-6 (also called MOF-545(Fe) or PCN-222(Fe)) was applied for the oxidation of 1,2,3-trihydroxybenzene (THB) and 2,2′-azinodi(3-ethylbenzothiazoline)-6-sulfonate (ABTS) with H_2O_2 (Scheme 4) [101]. The catalytic activity of MMPF-6 was compared with MMPF-6(Fr) with no metal ions inside the porphyrin units, and heme protein myoglobin (Mb) in ethanol solution. MMPF-6 showed the higher initial rates for the products purpurogallin and $ABTS^{\bullet+}$ formation than Mb (molecules agglomeration detected) and was re-usable for four recycles. PCN-222(Fe) was also applied

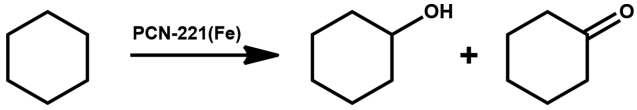

Scheme 5. Oxidation of cyclohexane.

to oxidate pyrogallol, 3,3,5,5-tetramethylbenzidine, and *o*-phenylenediamine in aqueous media [44]. The catalytic activity of PCN-222(Fe) was much higher than the hemin and horseradish peroxidase (HRP) enzyme.

PCN-221(Fe) was tested for selective oxidation of cyclohexane to cyclohexanone and cyclohexanol (K/A oil) (Scheme 5), the key chemical intermediates for the nylon production. The catalytic reaction was conducted with tert-butyl hydroperoxide (TBHP) at 65 °C. After 11 h, the product yield of 86.9% cyclohexanone and 5.4% cyclohexanol were obtained [50]. PCN-222(Fe)-F_7 functionalized with heptafluorobutyric acid (F_7) was also applied in the presence of TBHP and $AgBF_4$ under 1 bar O_2 at 80 °C for 24 h [24]. The added $AgBF_4$ replaces the Cl atom on the iron(III)-porphyrin ligand in the MOF for improved catalytic activity. PCN-222(Fe)-F_7 showed reasonable cyclohexane conversion (50.2%), KA oil selectivity (90%), and yield of KA oil (46.2%) with an optimal amount of TBHP (5.5 mM). Excessive TBHP could cause oxidative destruction of the MOF.

5. Hydroxylation

Several MOFs have been reported for their effectiveness on chemical warfare agents (CWAs) degradation (Scheme 6) with short half-lives (~2.5 min for dimethyl-4-nitrophenyl phosphate (DMNP) by MOF-525) [73]. However, the powder form of MOFs has limitations for direct applications. To increase applicability, polypropyl-

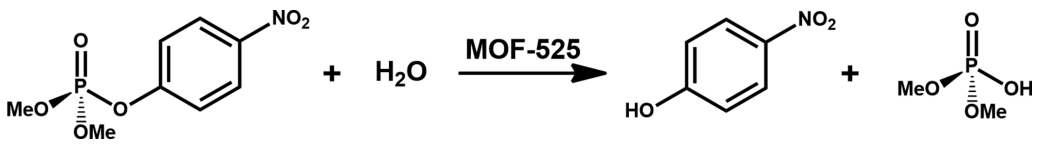

Scheme 6. Hydroxylation of dimethyl-4-nitrophenyl phosphate (DMNP).

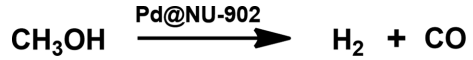

Scheme 7. Dehydrogenation of methanol.

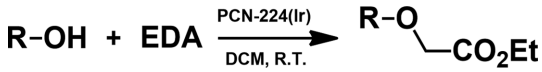

Scheme 8. Catalytic O-H insertion.

ene (PP)/metal oxides (Al_2O_3, TiO_2, ZnO, HfO_2, or ZrO_2)/MOF-525 composites were prepared for degradation of DMNP in *n*-ethyl morpholine buffer [73]. PP/TiO_2/MOF-525 (16% MOF loading) showed ~80 min half-life for degradation of DMNP. Defect sites in Zr-based MOFs are known as catalytically active sites for CWAs degradation, and their quantification by a suitable characterization method is necessary to establish the structure-activity relationship [102].

6. Dehydrogenation

Pd nanoparticles immobilized on three Zr-based MOFs of UiO-66, NU-902, and PCN-222 were tested for the catalytic dehydrogenation of methanol (Scheme 7) [69]. H_2 production rates increased 3.3 (PCN-222), 3.6 (NU-902), and 12.1 (UiO-66) mmol $(g\ Pd)^{-1}\ min^{-1}$ at 150 °C with the smaller Pd nanoparticles.

7. O-H Insertion

PCN-224(Ir) was prepared using a metalloporphyrin tetracarboxylic ligand Ir(TCPP)Cl and applied for the O-H insertion reaction of alcohols or phenols with ethyl diazoacetate (EDA) at room temperature for 10 min (Scheme 8) [103]. The product yield was 94% and 70% for isopropanol (^{i}PrOH) and 4-bromophenol, respectively. The catalytic activity of PCN-224(Ir) for ^{i}PrOH was higher than the homogeneous Ir(TPP)(CO)Cl (88%), and the Ir open metal sites and the large uniform pores in PCN-224(Ir) were proposed for its superior catalytic activity. The reusability showed steady conversions (88-94%) until the 9th and declined to 64% in the 10th run.

8. Hetero-Diels-Alder Reaction

The hetero-Diels-Alder (hDA) reaction dealing with the cycloaddition of aldehydes to dienes has been widely used to produce natural products. It requires strong Brønsted or Lewis acid sites, and only limited research has been reported with the unactivated aldehydes and simple dienes. The cationic Fe(III) porphyrin in PCN-223(Fe) exhibiting a strong affinity for all electron-donating species was generated by adding $AgBF_4$ during the hDA reaction (Scheme 9) [51]. The product yield was 99% for the reaction with benzaldehyde and 2,3-dimethyl-1,3-butadiene, and the catalytic activity was maintained during five cycles.

CATALYTIC APPLICATIONS (II): PHOTOCATALYSIS

1. CO_2 Reduction

Excessive CO_2 emission to the atmosphere resulting from burning fossil fuels causes global climate change. Thus, much effort for CO_2 capture, storage, and utilization has been made to remedy the situation [104-106]. Photocatalytic CO_2 reduction is an attractive approach that can convert CO_2 into valuable fuels and chemicals using solar energy over a photocatalyst. For Zr-based porphyrinic MOFs, the CO_2 reduction reaction starts from the formation of photogenerated electrons and holes located between the highest occupied molecular orbitals (HOMO) and the lowest occupied molecular orbitals (LUMO) in porphyrin ligand under light irradiation. After charge separation, the photogenerated electrons on the LUMO transfer to the catalytic reaction centers to react with adsorbed CO_2, as shown in Fig. 17. At this stage, the LUMO energy level must be located above the redox potential for the CO_2 reduction reaction, which depends on the formed product from CO_2. For example, the redox potential for the reduction of CO_2 to CO is −3.50 eV, while for methane, formic acid, and methanol are −3.79, −3.42, and −3.65 eV, respectively [107-109].

Jiang et al. initially explored the light-driven reduction of CO_2 using Zr-based porphyrinic MOFs [110]. The photocatalytic CO_2 reduction under visible light irradiation was realized over a photoactive porphyrin-based semiconductor-like MOF of PCN-222, which exhibited much higher activity than the precursor ligand of PCN-222 alone. The high CO_2 uptake capacity of MOF allowed it to interact more efficiently with CO_2 in acetonitrile (solvent), leading to improved photocatalytic conversion. Time-resolved transient absorption and photoluminescence spectroscopy confirmed the emergence of an extremely long-lived electron trap state in PCN-222, suppressing the detrimental electron-hole recombination, thereby increasing the photocatalytic CO_2 reduction efficiency. In the case of MOF-525(Co), atomically dispersed catalytic centers exhibited significantly enhanced photocatalytic conversion of CO_2, which showed a 3.13-fold improvement in CO evolution rate (200.6 $\mu mol\ g^{-1}\ h\ \mu^1$) and a 5.93-fold enhancement in CH_4 generation rate (36.67 $\mu mol\ g^{-1}\ h^{-1}$) compared with the parent MOF-525 [111]. As demonstrated by an energy transfer efficiency investigation and first-principles simulations, photogenerated electrons can be effectively transferred to the active sites, which facilitates charge separation in the semiconducting MOFs and supplies energetic electrons to gas molecules adsorbed on the MOFs. After incorporating the active sites, CO_2 can be easily captured and photocatalytically reduced into CO and CH_4 with dramatically improved performance in terms of both activity and CH_4 selectivity. Wang's group, via direct integration of PCN-224(Cu) and TiO_2 nanoparticles, established

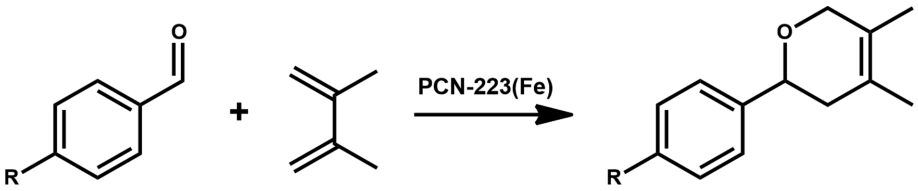

Scheme 9. Hetero-Diels-Alder reaction.

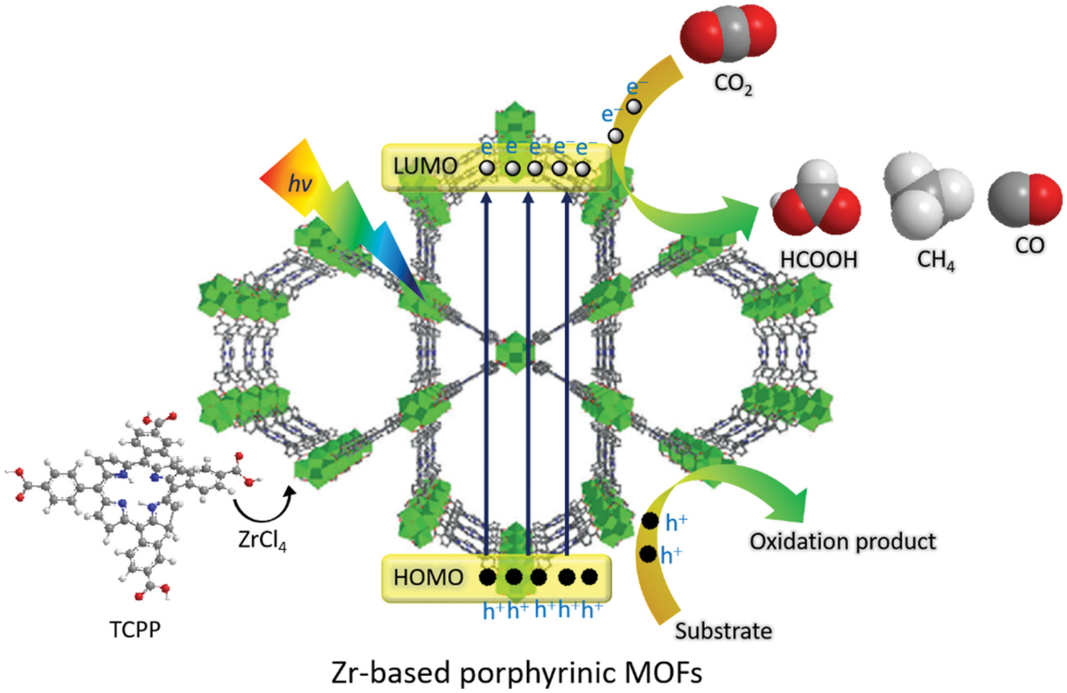

Fig. 17. Process of photocatalytic CO_2 reduction over Zr-based porphyrinic MOFs.

an efficient photocatalytic system capable of enhancing the catalytic activity of TiO_2 in CO_2 photoreduction [71]. In the absence of either co-catalyst or sacrificial reagent, the CO evolution rate could reach up to 37.21 μmol g^{-1} h^{-1}, ca. 10- and 45.4-times that of PCN-224(Cu) (3.72 μmol g^{-1} h^{-1}) and TiO_2 (0.82 μmol g^{-1} h^{-1}), respectively. Two contributing factors for the improvement were proposed: (1) the augmented ability of light-harvesting given by the integrated metalloporphyrin-based MOF and (2) the conjunction formed between the MOF and TiO_2, which constructs a Z-scheme mechanism favoring beneficial promotion on the separation of photoexcited charges.

2. Oxidation and Degradation

Singlet oxygen ($^1O_2$) is a reactive oxygen species (ROS) that plays a vital role in many physiological processes in living systems and acts as an excellent oxidizing agent in various organic reactions. Due to its high oxidation efficiency, sustainability, and convenience in separation, singlet oxygen has been widely used in organic synthesis [112]. $^1O_2$ is usually produced by photosensitization or chemical reactions. Commonly used photosensitizers include transition metal complexes, organic dyes, and porphyrin derivatives, transferring electronic energy from a triplet excited state to ground state triplet oxygen. However, there are some intrinsic drawbacks associated with these compounds, such as photo-bleaching and toxicity. To solve this problem, Zr-based porphyrinic MOFs were used in photocatalytic oxidation reactions. These Zr-based porphyrinic MOFs are not subject to photo-degradation due to their dense structure and also easily recoverable.

Bisphenol A (BPA) is one of the endocrine-disrupting chemicals [113]. PCN-222 showed a high BPA adsorption and subsequent photodegradation of BPA [91]. The lowest excited state oxygen molecule $^1O_2$ generated from PCN-222 oxidized BPA under visible-light, which exhibited the degradation rate of 0.004 mg/min within 20 min. 1,4-benzoquinone intermediate product only was observed during the photodegradation process. High removal efficiency (99.2%) for BPA adsorption and degradation was maintained during the five cycles tested.

At room temperature and neutral pH, singlet oxygen was generated by PCN-222 using a commercially available light-emitting diode. The singlet oxygen produced by PCN-222 selectively oxidized 2-chloroethyl ethyl sulfur (CEES) to the comparatively nontoxic 2-chloroethyl ethyl sulfoxide (CEESO) without formation of highly toxic sulfone [114]. In addition to the $^1O_2$ generation, the high surface areas and permanent porosities of MOFs can enhance the adsorption of toxic chemical agents and accelerate the catalytic process, rendering MOFs useful for the detoxification of CWAs. Thus, nanocrystals of PCN-222 were used as a dual-function catalyst for the simultaneous detoxification of two CWA simulants at room temperature. Simulants of nerve agent (GD and VX) and mustard gas (DMNP and CEES) were hydrolyzed and oxidized, respectively, to nontoxic products via a pair of catalyzed pathways [115]. Under visible (blue LED) irradiation, nanosized PCN-222 could simultaneously hydrolyze DMNP and oxidize CEES to nontoxic products in one system, with half-lives of 8 and 12 min, respectively.

The selectivity control to the aldehyde in aromatic alcohol oxidation using molecular oxygen under mild conditions remains a challenge. Pt/PCN-224(Zn) composites exhibited excellent catalytic performance in the photooxidation of aromatic alcohols by O_2 at ambient temperature at 1 atm due to a synergetic photothermal effect and singlet oxygen production [70]. Furthermore, the injection of hot electrons from the plasmonic Pt into PCN-224(Zn) would lower the electron density of the Pt nanocrystal surface, which

is the active site of benzyl alcohol oxidation. Thus, it was possible to tailor the material for the optimized catalytic performance via the competition between the Schottky junction (electron transfer from PCN-224(Zn) to Pt) and the plasmonic effect (electron transfer from Pt to PCN-224(Zn)) by altering the light intensity.

Upon visible light irradiation in benzylamine, PCN-222 initiated charge separation, generating oxygen-centered active sites in Zr-oxo clusters. The photogenerated electrons and holes activated oxygen and amines, respectively, to give the corresponding redox products [116]. The direct oxidative coupling from benzylamines to *N*-benzylidenebenzylamine via $^1O_2$ generated by the porphyrin ligand and the synergistic effect between the charge transfer-induced electrons and holes contributed to the reaction. PCN-222 exhibited excellent photocatalytic activity, selectivity, and recyclability toward this reaction.

Fe@PCN-224 exhibited significant photocatalytic activity in isopropanol (IPA) photooxidation, which was equivalent to an 8.9-fold improvement in acetone evolution rate and a 9.3-fold enhancement in CO_2 generation rate compared with PCN-224 [117]. The implantation of Fe(III) ions in PCN-224 not only improved the separation efficiency of photogenerated electron-hole pairs but also induced Fenton reactions to convert in-situ formed H_2O_2 into reactive radicals (such as $\cdot O_2^-$ and ·OH), which play a significant role in the oxidation of IPA. Fe@PCN-222 showed enhanced activity for photocatalytic oxidation of IPA compared with bare PCN-222. The MOF with Fe-metallated in both Zr clusters and porphyrin ligands, Fe@PCN-222(Fe) showed catalytic activity for one-pot tandem synthesis of quinazolin-4(3*H*)-ones from alcohols and 2-aminobenzamide through a three-consecutive step reaction (oxidation-cyclization-oxidation) under visible light irradiation using air or oxygen without adding any additive [62].

3. H_2 Generation

Storing solar energy in the chemical bonds of fuel is highly desirable. H_2 is the simplest such 'solar fuel', and it can be generated from water via electrolysis or semiconductor photocatalysts that absorb light, converting it to electrical charges that drive surface redox reactions. A system in which photocatalysts are directly dispersed in water is the cheapest way to produce solar H_2 [118]. Feng's group devised a new biomimetic heterogeneous hydrogen evolution photocatalyst ([FeFe]@MOF-545(Zn)) [67]. The immobilized biomimetic $[Fe_2S_2]$ inside the MOF-545(Zn) shows significant improvement in hydrogen generation compared with the reference homogeneous catalyst $[(i\text{-}SCH_2)_2NC(O)C_5H_4N]\text{-}[Fe_2(CO)_6]$. Due to the enhanced stability of the di-iron catalyst inside the highly stable MOF structure, [FeFe]@MOF-545(Zn) exhibited higher efficiency in photochemical hydrogen evolution than the similar molecular catalyst in terms of rate and total hydrogen production yield.

Finally, photodynamic therapy (PDT) using a porphyrinic MOF can be a safe and convenient method for cancer treatment, in which $^1O_2$ generated is involved in oxidative damage on cancer cells [119]. The size-controlled PCN-224 (90 nm) functionalized with folic acid (FA) onto the unsaturated sites of the Zr_6 cluster was investigated for PDT [42], and a porphyrinic MOF with a high content of porphyrin (59.8%) and doxorubicin (109%) was also reported effective [120].

CATALYTIC APPLICATIONS (III): ELECTROCATALYSIS

1. CO_2 Reduction

Iron porphyrin complexes have been well known and extensively studied for electrocatalytic CO_2 reduction to CO with the Fe (0)-porphyrin being the active sites [121]. Hod et al. prepared MOF-525 on fluorine-doped tin oxide (FTO) as a thin film and post-metallated it with iron chloride to generate redox-conductivity in high surface coverage of catalytic sites for CO_2 reduction [28]. The MOF catalytic film (6.2×10^{-8} mol/cm^2) was subjected to controlled potential electrolysis (CPE) (−1.3 V versus NHE) in 1 M tetrabutylammonium hexafluorophosphate ($TBAPF_6$) acetonitrile electrolyte solution saturated with CO_2. The thin film reached 2.3 mA/cm^2 current density in 30 min and generated 15.3 and 14.9 μmol/cm^2 for CO and H_2, respectively, after 4 h.

2. Oxidation

Detecting trace amounts of nitrite is necessary for the food industry and medical diagnosis. MOF-525 in different particle sizes (100-700 nm) was synthesized and formed into thin films using the inkjet-printing method for electrocatalytic nitrite oxidation [41]. A cyclic voltammetry (CV) curve was obtained in 0.1 M KCl solution (pH: 7.0) at room temperature using the MOF-525 thin film as the working electrode. In general, thin films with smaller MOF-525 particles showed better electrocatalytic activity. It was tested for an amperometric nitrite senor, and the linear range, sensitivity, and detection limit of the sensor were 10-800 μM, 40.6 μA mM^{-1} cm^{-2}, and 0.72 μM, respectively. Nanocomposites of MOF-525 and graphene nanoribbons (GNRs) were prepared for electrocatalytic oxidation of nitrite by adding different amounts of GNRs during MOF-525 synthesis [77]. A thin film of MOF-GNRs-50 (GNRs: 50 mg) showed a significantly higher current density than pristine MOF-525 or GNRs. For an amperometric nitrite sensor, the linear range, sensitivity, and detection limit were 100-2,500 μM, 93.8 μA mM^{-1} cm^{-2}, and 0.75 μM at 0.85 V vs. Ag/AgCl/KCl (saturated).

3. Oxygen Reduction Reaction (ORR)

The coordinatively unsaturated metal atoms in SACs show excellent catalytic performance. Jiang's group reported two Fe_{SA}-N-C samples by pyrolysis of PCN-222(Fe) and evaluated it for ORR. The Fe_{SA}-N-C sample derived from pyrolysis of a mixed ligand synthesis PCN-222(Fe) showed 23.27 mA cm^{-2} of kinetic current density (J_k). Similarly, a Fe_{SA}-N-C sample derived from pyrolysis of SiO_2-casted PCN-222(Fe) showed 37.19 mA cm^{-2} at 0.85 V in 0.1 M KOH [86,88]. Both Fe_{SA}-N-C samples showed superior ORR performance to other metal catalysts, including the Pt/C, in acidic and alkaline media due to single-atom iron sites' superior activity, hierarchical porous environment, and high conductivity of carbon.

4. Nitrogen Reduction Reaction (NRR)

The electrochemical NRR deals with ammonia production from N_2, H_2O, and electricity at ambient conditions. M_1-N-C materials (single site catalysts) were prepared by pyrolysis of the mixed ligand synthesis PCN-222(M) (M: Fe, Co, or Ni) for electrocatalytic NRR (and competing H_2 evolution reaction) [55]. Among the catalysts, Fe_1-N-C showed the highest catalytic activity for NH_3 production (compared with Co_1-N-C or Ni_1-N-C), including faradaic effi-

ciency of 4.51% and a product yield rate of 1.56×10^{-11} mol cm^{-2} s^{-1} at −0.05 V because of the advantages of Fe_1-N-C material mentioned above for ORR. Density-functional theory (DFT) calculation also indicated that Fe_1-N-C has the lowest energy barrier of the rate-determining step during the NRR process.

CONCLUDING REMARKS

Many porphyrinic MOFs have been synthesized with various porphyrin ligands and transition metal ion clusters. The porphyrinic MOFs have isolated porphyrin units imbedded in MOFs' rigid porous structure, functioning as active sites for various applications. Among the porphyrin ligands, tetrakis(4-carboxyphenyl)-porphyrin (TCPP) is broadly employed to synthesize porphyrinic MOFs composed of metal ions of Zr, Cu, Mn, In, Al, or Fe. In particular, Zr-based porphyrinic MOFs, owing to their excellent textural properties and high stability, are drawing attention. The Zr-based porphyrinic MOFs of MOF-525, MOF-545 (also named PCN-222), PCN-221, PCN-223, PCN-224, PCN-225, and NU-902 have been reported.

In this short review, we have summarized the recent development in synthesis, characterization, functionalization, and applications in adsorption and catalysis of the Zr-based porphyrinic MOFs. Extensive efforts have been made to synthesize the pure phase MOFs and functionalize them to enhance their properties for various applications. The well-dispersed metalloporphyrin units over a stable MOF structure, coordination-unsaturated Zr clusters, and functional groups introduced to the MOF, aided by the high porosity in Zr-based porphyrinic MOFs, demonstrated their significant potential as adsorbents, sensors, heterogeneous catalysts for chemical conversions and photocatalysts. Pyrolysis of the Zr-based porphyrinic MOFs can convert them to N-doped carbons deposited with different metal oxides, which is being developed into a new scientific tool for clean energy and sustainability such as electrocatalysts and supercapacitors.

From this review, the following conclusions and suggestions for further research work can be made:

(1) Many synthesis works have been reported to prepare phase-pure Zr-based porphyrinic MOFs, and some success has been achieved by selecting a suitable modulator which guides the nucleation and by optimizing the synthesis conditions. MOF-525 and MOF-545 seem to be the material of high interest among the seven Zr-based porphyrinic MOFs with different topologies. However, additional synthesis work is still necessary for their facile synthesis. It takes too long a synthesis time (several days) for a only small amount of product. Reproducible synthesis methods for pure and uniform particles on a large scale are lacking. The following synthesis methods can also be an option: microwave-assisted, sonochemical, electrochemical, mechanochemical, microfluidic, and dry-gel synthesis. So far, only limited work on microwave-assisted synthesis has been reported, and our preliminary work on sono-synthesis shows some promise.

(2) The defect sites are formed during the synthesis of Zr-based porphyrinic MOFs. These are vacancies of the linker or/and metal clusters in the structure, and function as the catalytic active sites for the decomposition of warfare chemical agents. Modulator acidity and amounts are established as the critical factors for their formation. The clear mechanism of the defect site formation and objective characterization methods should be established for future catalytic applications.

(3) Diverse introduction of organic and inorganic species onto the Zr-based porphyrinic MOFs has been reported: metalation, grafting, impregnation, composites, and pyrolysis. Currently, porphyrin metalation (both pre- and post-synthesis methods) requires a large amount of metal source in excess (ca. 5 times the stoichiometric amount). A more efficient metalation method would be desirable. Grafting onto the zirconium sites is common, whereas little work has been done on the grafting on the metallated sites in the porphyrin units. Important work on the formation of MOF particles on various support materials has been done, which will expand the scope of applications for the MOFs in general.

(4) Zr-based porphyrinic MOFs are increasingly investigated as adsorbents utilizing the porphyrin units' unique chemical properties incorporated into the water-stable MOF structure. The removal of various aqueous organic pollutants was confirmed. Light gas separation, including CO_2, was reported but their effectiveness compared with other adsorbent materials seem questionable. On the other hand, fluorescence detection of hazardous species utilizing the porphyrin units in the MOFs and performance evaluation of the adsorption cooling system using the Zr-based porphyrinic MOFs and ethanol pair look promising.

(5) Many successful catalytic applications of Zr-based porphyrinic MOFs have been reported. For heterogeneous catalysis for chemical conversion, their use for cascade reactions seems promising because it is possible to generate multi-catalytic active sites in the single MOF using various functionalization. Biomimetic catalysis also needs to be explored more, making use of the porphyrin functionality with metal oxide clusters. Photocatalysis using the Zr-based porphyrinic MOFs has excellent potential due to the porphyrin's visible light reception and various possibilities provided by the metals introduced. Electrocatalysis by the pyrolyzed Zr-based porphyrinic MOFs also has good potential for sustainability applications.

(6) It is desirable to synthesize Zr-based MOF structures comprised of new porphyrin units other than TCCP, since the porphyrin structures strongly influence the catalytic property of the metallated MOFs. Organic functionalization on the commercially available porphyrin ligands needs to be expanded for the synthesis of new Zr-based MOF structures and composite materials.

ACKNOWLEDEGEMENTS

This work was supported by the National Research Foundation of Korea (NRF) funded by the Ministry of Science and ICT (No. 2020R1A2C1011381).

REFERENCES

1. Y.-R. Lee, J. Kim and W.-S. Ahn, *Korean J. Chem. Eng.*, **30**, 1667 (2013).
2. B. Li, H. M. Wen, Y. Cui, W. Zhou, G. Qian and B. Chen, *Adv. Mater.*, **28**, 8819 (2016).

3. R. B. Getman, Y. S. Bae, C. E. Wilmer and R. Q. Snurr, *Chem. Rev.*, **112**, 703 (2012).
4. S. Qiu, M. Xue and G. Zhu, *Chem. Soc. Rev.*, **43**, 6116 (2014).
5. J. Lee, O. K. Farha, J. Roberts, K. A. Scheidt, S. T. Nguyen and J. T. Hupp, *Chem. Soc. Rev.*, **38**, 1450 (2009).
6. L. E. Kreno, K. Leong, O. K. Farha, M. Allendorf, R. P. Van Duyne and J. T. Hupp, *Chem. Rev.*, **112**, 1105 (2012).
7. P. Horcajada, T. Chalati, C. Serre, B. Gillet, C. Sebrie, T. Baati, J. F. Eubank, D. Heurtaux, P. Clayette, C. Kreuz, J. S. Chang, Y. K. Hwang, V. Marsaud, P. N. Bories, L. Cynober, S. Gil, G. Ferey, P. Couvreur and R. Gref, *Nat. Mater.*, **9**, 172 (2010).
8. Y. V. Kaneti, J. Tang, R. R. Salunkhe, X. Jiang, A. Yu, K. C. Wu and Y. Yamauchi, *Adv. Mater.*, **29**, 1604898 (2017).
9. Q. L. Zhu and Q. Xu, *Chem. Soc. Rev.*, **43**, 5468 (2014).
10. S. Yuan, L. Feng, K. Wang, J. Pang, M. Bosch, C. Lollar, Y. Sun, J. Qin, X. Yang, P. Zhang, Q. Wang, L. Zou, Y. Zhang, L. Zhang, Y. Fang, J. Li and H. C. Zhou, *Adv. Mater.*, **30**, 1704303 (2018).
11. T. F. Liu, D. Feng, Y. P. Chen, L. Zou, M. Bosch, S. Yuan, Z. Wei, S. Fordham, K. Wang and H. C. Zhou, *J. Am. Chem. Soc.*, **137**, 413 (2015).
12. S. Yuan, J. S. Qin, C. T. Lollar and H. C. Zhou, *ACS Cent. Sci.*, **4**, 440 (2018).
13. M. Kim and S. M. Cohen, *CrystEngComm.*, **14**, 4096 (2012).
14. S. Bhattacharjee, C. Chen and W.-S. Ahn, *RSC Adv.*, **4**, 52500 (2014).
15. S. Huh, S.-J. Kim and Y. Kim, *CrystEngComm.*, **18**, 345 (2016).
16. W. Y. Gao, M. Chrzanowski and S. Ma, *Chem. Soc. Rev.*, **43**, 5841 (2014).
17. N. U. Day, C. C. Wamser and M. G. Walter, *Polym. Int.*, **64**, 833 (2015).
18. L. Meng, Q. Cheng, C. Kim, W. Y. Gao, L. Wojtas, Y. S. Chen, M. J. Zaworotko, X. P. Zhang and S. Ma, *Angew. Chem. Int. Ed.*, **51**, 10082 (2012).
19. W. Y. Gao, L. Wojtas and S. Ma, *Chem. Commun.*, **50**, 5316 (2014).
20. M. H. Xie, X. L. Yang, C. Zou and C. D. Wu, *Inorg. Chem.*, **50**, 5318 (2011).
21. H. J. Son, S. Jin, S. Patwardhan, S. J. Wezenberg, N. C. Jeong, M. So, C. E. Wilmer, A. A. Sarjeant, G. C. Schatz, R. Q. Snurr, O. K. Farha, G. P. Wiederrecht and J. T. Hupp, *J. Am. Chem. Soc.*, **135**, 862 (2013).
22. Z. Guo, D. Yan, H. Wang, D. Tesfagaber, X. Li, Y. Chen, W. Huang and B. Chen, *Inorg. Chem.*, **54**, 200 (2015).
23. L. Xu, J. Wang, Y. Xu, Z. Zhang, P. Lu, M. Fang, S. Li, P. Sun and H.-K. Liu, *CrystEngComm.*, **16**, 8656 (2014).
24. L. Li, Q. Yang, S. Chen, X. Hou, B. Liu, J. Lu and H. L. Jiang, *Chem. Commun.*, **53**, 10026 (2017).
25. L. Feng, K.-Y. Wang, E. Joseph and H.-C. Zhou, *Trends Chem.*, **2**, 555 (2020).
26. H. Li, F. Zhai, D. Gui, X. Wang, C. Wu, D. Zhang, X. Dai, H. Deng, X. Su, J. Diwu, Z. Lin, Z. Chai and S. Wang, *Appl. Catal. B: Environ.*, **254**, 47 (2019).
27. J. W. Brown, Q. T. Nguyen, T. Otto, N. N. Jarenwattananon, S. Glöggler and L.-S. Bouchard, *Catal. Commun.*, **59**, 50 (2015).
28. I. Hod, M. D. Sampson, P. Deria, C. P. Kubiak, O. K. Farha and J. T. Hupp, *ACS Catal.*, **5**, 6302 (2015).
29. J. Yang, Z. Wang, K. Hu, Y. Li, J. Feng, J. Shi and J. Gu, *ACS Appl. Mater. Interfaces*, **7**, 11956 (2015).
30. K. Yu, I. Ahmed, D. I. Won, W. I. Lee and W. S. Ahn, *Chemosphere*, **250**, 126133 (2020).
31. A. Umemura, S. Diring, S. Furukawa, H. Uehara, T. Tsuruoka and S. Kitagawa, *J. Am. Chem. Soc.*, **133**, 15506 (2011).
32. K. Wang, D. Feng, T. F. Liu, J. Su, S. Yuan, Y. P. Chen, M. Bosch, X. Zou and H. C. Zhou, *J. Am. Chem. Soc.*, **136**, 13983 (2014).
33. M. L. Kelty, W. Morris, A. T. Gallagher, J. S. Anderson, K. A. Brown, C. A. Mirkin and T. D. Harris, *Chem. Commun.*, **52**, 7854 (2016).
34. P. Li, R. C. Klet, S. Y. Moon, T. C. Wang, P. Deria, A. W. Peters, B. M. Klahr, H. J. Park, S. S. Al-Juaid, J. T. Hupp and O. K. Farha, *Chem. Commun.*, **51**, 10925 (2015).
35. B. L. Bonnett, E. D. Smith, M. De La Garza, M. Cai, J. V. t. Haag, J. M. Serrano, H. D. Cornell, B. Gibbons, S. M. Martin and A. J. Morris, *ACS Appl. Mater. Interfaces*, **12**, 15765 (2020).
36. Y. Bai, Y. Dou, L. H. Xie, W. Rutledge, J. R. Li and H. C. Zhou, *Chem. Soc. Rev.*, **45**, 2327 (2016).
37. S. Bao, X. Cai, Y. Shi and M. Pang, *CrystEngComm.*, **19**, 1875 (2017).
38. S. M. Shaikh, P. M. Usov, J. Zhu, M. Cai, J. Alatis and A. J. Morris, *Inorg. Chem.*, **58**, 5145 (2019).
39. H. Q. Xu, K. Wang, M. Ding, D. Feng, H. L. Jiang and H. C. Zhou, *J. Am. Chem. Soc.*, **138**, 5316 (2016).
40. X. Gong, H. Noh, N. C. Gianneschi and O. K. Farha, *J. Am. Chem. Soc.*, **141**, 6146 (2019).
41. C.-H. Su, C.-W. Kung, T.-H. Chang, H.-C. Lu, K.-C. Ho and Y.-C. Liao, *J. Mater. Chem. A.*, **4**, 11094 (2016).
42. J. Park, Q. Jiang, D. Feng, L. Mao and H. C. Zhou, *J. Am. Chem. Soc.*, **138**, 3518 (2016).
43. S. Carrasco, A. Sanz-Marco and B. Martín-Matute, *Organometallics*, **38**, 3429 (2019).
44. D. Feng, Z. Y. Gu, J. R. Li, H. L. Jiang, Z. Wei and H. C. Zhou, *Angew. Chem. Int. Ed.*, **51**, 10307 (2012).
45. P. Deria, D. A. Gomez-Gualdron, I. Hod, R. Q. Snurr, J. T. Hupp and O. K. Farha, *J. Am. Chem. Soc.*, **138**, 14449 (2016).
46. K. C. Park, C. Seo, G. Gupta, J. Kim and C. Y. Lee, *ACS Appl. Mater. Interfaces*, **9**, 38670 (2017).
47. Y. C. Qiu, S. Yuan, X. X. Li, D. Y. Du, C. Wang, J. S. Qin, H. F. Drake, Y. Q. Lan, L. Jiang and H. C. Zhou, *J. Am. Chem. Soc.*, **141**, 13841 (2019).
48. S. Yuan, J. S. Qin, L. Zou, Y. P. Chen, X. Wang, Q. Zhang and H. C. Zhou, *J. Am. Chem. Soc.*, **138**, 6636 (2016).
49. W. Morris, B. Volosskiy, S. Demir, F. Gandara, P. L. McGrier, H. Furukawa, D. Cascio, J. F. Stoddart and O. M. Yaghi, *Inorg. Chem.*, **51**, 6443 (2012).
50. D. Feng, H. L. Jiang, Y. P. Chen, Z. Y. Gu, Z. Wei and H. C. Zhou, *Inorg. Chem.*, **52**, 12661 (2013).
51. D. Feng, Z. Y. Gu, Y. P. Chen, J. Park, Z. Wei, Y. Sun, M. Bosch, S. Yuan and H. C. Zhou, *J. Am. Chem. Soc.*, **136**, 17714 (2014).
52. D. Feng, W. C. Chung, Z. Wei, Z. Y. Gu, H. L. Jiang, Y. P. Chen, D. J. Darensbourg and H. C. Zhou, *J. Am. Chem. Soc.*, **135**, 17105 (2013).
53. H. L. Jiang, D. Feng, K. Wang, Z. Y. Gu, Z. Wei, Y. P. Chen and H. C. Zhou, *J. Am. Chem. Soc.*, **135**, 13934 (2013).
54. E. Moradi, R. Rahimi and V. Safarifard, *J. Solid State Chem.*, **286**, (2020).
55. R. Zhang, L. Jiao, W. Yang, G. Wan and H.-L. Jiang, *J. Mater. Chem.*

A., **7**, 26371 (2019).
56. Z. Fang, B. Bueken, D. E. De Vos and R. A. Fischer, *Angew. Chem. Int. Ed.*, **54**, 7234 (2015).
57. H. Wu, Y. S. Chua, V. Krungleviciute, M. Tyagi, P. Chen, T. Yildirim and W. Zhou, *J. Am. Chem. Soc.*, **135**, 10525 (2013).
58. G. C. Shearer, S. Chavan, S. Bordiga, S. Svelle, U. Olsbye and K. P. Lillerud, *Chem. Mater.*, **28**, 3749 (2016).
59. C. C. Epley, M. D. Love and A. J. Morris, *Inorg. Chem.*, **56**, 13777 (2017).
60. G. Barin, V. Krungleviciute, O. Gutov, J. T. Hupp, T. Yildirim and O. K. Farha, *Inorg. Chem.*, **53**, 6914 (2014).
61. S. Bhattacharjee, M.-S. Jang, H.-J. Kwon and W.-S. Ahn, *Catal. Surv. Asia*, **18**, 101 (2014).
62. M. R. Ghaleno, M. Ghaffari-Moghaddam, M. Khajeh, A. Reza Oveisi and M. Bohlooli, *J. Colloid Interface Sci.*, **535**, 214 (2019).
63. W. Jumpathong, T. Pila, Y. Lekjing, P. Chirawatkul, B. Boekfa, S. Horike and K. Kongpatpanich, *APL Mater.*, **7**, 111109 (2019).
64. P. Deria, W. Bury, I. Hod, C. W. Kung, O. Karagiaridi, J. T. Hupp and O. K. Farha, *Inorg. Chem.*, **54**, 2185 (2015).
65. P. Deria, J. E. Mondloch, E. Tylianakis, P. Ghosh, W. Bury, R. Q. Snurr, J. T. Hupp and O. K. Farha, *J. Am. Chem. Soc.*, **135**, 16801 (2013).
66. K. Yu, P. Puthiaraj and W.-S. Ahn, *Appl. Catal. B: Environ.*, **273**, (2020).
67. K. Sasan, Q. Lin, C. Mao and P. Feng, *Chem. Commun.*, **50**, 10390 (2014).
68. G. Lu, S. Li, Z. Guo, O. K. Farha, B. G. Hauser, X. Qi, Y. Wang, X. Wang, S. Han, X. Liu, J. S. DuChene, H. Zhang, Q. Zhang, X. Chen, J. Ma, S. C. Loo, W. D. Wei, Y. Yang, J. T. Hupp and F. Huo, *Nat. Chem.*, **4**, 310 (2012).
69. Y.-H. Wang, C.-H. Chuang, T.-A. Chiu, C.-W. Kung and W.-Y. Yu, *J. Phys. Chem. C.*, **124**, 12521 (2020).
70. Y. Z. Chen, Z. U. Wang, H. Wang, J. Lu, S. H. Yu and H. L. Jiang, *J. Am. Chem. Soc.*, **139**, 2035 (2017).
71. L. Wang, P. Jin, J. Huang, H. She and Q. Wang, *ACS Sustain. Chem. Eng.*, **7**, 15660 (2019).
72. S. Li and F. Huo, *Nanoscale*, **7**, 7482 (2015).
73. H. F. Barton, A. K. Davis and G. N. Parsons, *ACS Appl. Mater. Interfaces*, **12**, 14690 (2020).
74. X. Yang, S. Yuan, L. Zou, H. Drake, Y. Zhang, J. Qin, A. Alsalme and H. C. Zhou, *Angew. Chem. Int. Ed.*, **57**, 3927 (2018).
75. J. Zhao, D. T. Lee, R. W. Yaga, M. G. Hall, H. F. Barton, I. R. Woodward, C. J. Oldham, H. J. Walls, G. W. Peterson and G. N. Parsons, *Angew. Chem. Int. Ed.*, **55**, 13224 (2016).
76. D. T. Lee, J. D. Jamir, G. W. Peterson and G. N. Parsons, *Matter*, **2**, 404 (2020).
77. C.-W. Kung, Y.-S. Li, M.-H. Lee, S.-Y. Wang, W.-H. Chiang and K.-C. Ho, *J. Mater. Chem. A.*, **4**, 10673 (2016).
78. N. Huang, H. Drake, J. Li, J. Pang, Y. Wang, S. Yuan, Q. Wang, P. Cai, J. Qin and H. C. Zhou, *Angew. Chem. Int. Ed.*, **57**, 8916 (2018).
79. L. Du, L. Xing, G. Zhang and S. Sun, *Carbon*, **156**, 77 (2020).
80. H. F. Wang, L. Chen, H. Pang, S. Kaskel and Q. Xu, *Chem. Soc. Rev.*, **49**, 1414 (2020).
81. L. Jiao and H.-L. Jiang, *Chem.*, **5**, 786 (2019).
82. M. C. Wasson, C. T. Buru, Z. Chen, T. Islamoglu and O. K. Farha, *Appl. Catal. A: Gen.*, **586**, 117214 (2019).
83. A. Han, B. Wang, A. Kumar, Y. Qin, J. Jin, X. Wang, C. Yang, B. Dong, Y. Jia, J. Liu and X. Sun, *Small Methods*, **3**, 1800471 (2019).
84. K. Shen, X. Chen, J. Chen and Y. Li, *ACS Catal.*, **6**, 5887 (2016).
85. Y.-R. Lee, H. Yoo, J. Choi and W.-S. Ahn, *Cellulose*, **27**, 2723 (2020).
86. L. Jiao, R. Zhang, G. Wan, W. Yang, X. Wan, H. Zhou, J. Shui, S. H. Yu and H. L. Jiang, *Nat. Commun.*, **11**, 2831 (2020).
87. T. H. Chang, C. Young, M. H. Lee, R. R. Salunkhe, S. M. Alshehri, T. Ahamad, M. T. Islam, K. C. Wu, M. S. A. Hossain, Y. Yamauchi and K. C. Ho, *Chem. Asian J.*, **12**, 2857 (2017).
88. L. Jiao, G. Wan, R. Zhang, H. Zhou, S. H. Yu and H. L. Jiang, *Angew. Chem. Int. Ed.*, **57**, 8525 (2018).
89. H. Li, X. Cao, C. Zhang, Q. Yu, Z. Zhao, X. Niu, X. Sun, Y. Liu, L. Ma and Z. Li, *RSC Adv.*, **7**, 16273 (2017).
90. M. Sarker, S. Shin, J. H. Jeong and S. H. Jhung, *Chem. Eng. J.*, **371**, 252 (2019).
91. A. N. Meng, L. X. Chaihu, H. H. Chen and Z. Y. Gu, *Sci. Rep.*, **7**, 6297 (2017).
92. C. Chen, Y.-R. Lee and W.-S. Ahn, *J. Nanosci. Nanotechnol.*, **16**, 4291 (2016).
93. J. Liu, P. K. Thallapally, B. P. McGrail, D. R. Brown and J. Liu, *Chem. Soc. Rev.*, **41**, 2308 (2012).
94. M. Ding, R. W. Flaig, H. L. Jiang and O. M. Yaghi, *Chem. Soc. Rev.*, **48**, 2783 (2019).
95. A. Boutin, S. Couck, F.-X. Coudert, P. Serra-Crespo, J. Gascon, F. Kapteijn, A. H. Fuchs and J. F. M. Denayer, *Micropor. Mesopor. Mater.*, **140**, 108 (2011).
96. D. Lv, R. Shi, Y. Chen, Y. Chen, H. Wu, X. Zhou, H. Xi, Z. Li and Q. Xia, *Ind. Eng. Chem. Res.*, **57**, 12215 (2018).
97. Z. Li, X. Li, C. Chen, L. Zhou, Q. Guo, D. Yuan, H. Wan, J. Ding and G. Guan, *Eur. J. Inorg. Chem.*, **2018**, 194 (2018).
98. R. Shi, D. Lv, Y. Chen, H. Wu, B. Liu, Q. Xia and Z. Li, *Sep. Purif. Technol.*, **207**, 262 (2018).
99. H. Chen, Z. Chen, L. Zhang, P. Li, J. Liu, L. R. Redfern, S. Moribe, Q. Cui, R. Q. Snurr and O. K. Farha, *Chem. Mater.*, **31**, 2702 (2019).
100. H. A. J. Hibbard, M. J. Burnley, H. N. Rubin, J. A. Miera and M. M. Reynolds, *Inorg. Chem. Commun.*, **115**, 107861 (2020).
101. Y. Chen, T. Hoang and S. Ma, *Inorg. Chem.*, **51**, 12600 (2012).
102. S. Y. Moon, Y. Liu, J. T. Hupp and O. K. Farha, *Angew. Chem. Int. Ed.*, **54**, 6795 (2015).
103. H. Cui, Y. Wang, Y. Wang, Y.-Z. Fan, L. Zhang and C.-Y. Su, *CrystEngComm.*, **18**, 2203 (2016).
104. W. H. Wang, Y. Himeda, J. T. Muckerman, G. F. Manbeck and E. Fujita, *Chem. Rev.*, **115**, 12936 (2015).
105. C. A. Trickett, A. Helal, B. A. Al-Maythalony, Z. H. Yamani, K. E. Cordova and O. M. Yaghi, *Nat. Rev. Mater.*, **2**, 17045 (2017).
106. E. S. Sanz-Perez, C. R. Murdock, S. A. Didas and C. W. Jones, *Chem. Rev.*, **116**, 11840 (2016).
107. J. W. Maina, C. Pozo-Gonzalo, L. Kong, J. Schütz, M. Hill and L. F. Dumée, *Mater. Horiz.*, **4**, 345 (2017).
108. S. Hamad, N. C. Hernandez, A. Aziz, A. R. Ruiz-Salvador, S. Calero and R. Grau-Crespo, *J. Mater. Chem. A.*, **3**, 23458 (2015).
109. A. Corma and H. Garcia, *J. Catal.*, **308**, 168 (2013).
110. H. Q. Xu, J. Hu, D. Wang, Z. Li, Q. Zhang, Y. Luo, S. H. Yu and H. L. Jiang, *J. Am. Chem. Soc.*, **137**, 13440 (2015).
111. H. Zhang, J. Wei, J. Dong, G. Liu, L. Shi, P. An, G. Zhao, J. Kong, X. Wang, X. Meng, J. Zhang and J. Ye, *Angew. Chem. Int. Ed.*, **55**,

14310 (2016).
112. A. Li, C. Tan, T. Yuan, J. Liang, D. Gao, Y. Tan and Y. Jiang, *J. Mater. Chem. A.*, **6**, 15927 (2018).
113. M. C. Prete and C. R. T. Tarley, *Chem. Eng. J.*, **367**, 102 (2019).
114. Y. Liu, A. J. Howarth, J. T. Hupp and O. K. Farha, *Angew. Chem. Int. Ed.*, **54**, 9001 (2015).
115. Y. Liu, S.-Y. Moon, J. T. Hupp and O. K. Farha, *ACS Nano*, **9**, 12358 (2015).
116. C. Xu, H. Liu, D. Li, J. H. Su and H. L. Jiang, *Chem. Sci.*, **9**, 3152 (2018).
117. L. Shi, L. Yang, H. Zhang, K. Chang, G. Zhao, T. Kako and J. Ye, *Appl. Catal. B: Environ.*, **224**, 60 (2018).
118. J. Kosco, M. Bidwell, H. Cha, T. Martin, C. T. Howells, M. Sachs, D. H. Anjum, S. G. Lopez, L. Zou, A. Wadsworth, W. Zhang, L. Zhang, J. Tellam, R. Sougrat, F. Laquai, D. M. DeLongchamp, J. R. Durrant and I. McCulloch, *Nat. Mater.*, **19**, 559 (2020).
119. Z. Hu, Y. Pan, J. Wang, J. Chen, J. Li and L. Ren, *Biomed. Pharmacother.*, **63**, 155 (2009).
120. W. Liu, Y. M. Wang, Y. H. Li, S. J. Cai, X. B. Yin, X. W. He and Y. K. Zhang, *Small*, **13**, (2017).
121. P. Sen, B. Mondal, D. Saha, A. Rana and A. Dey, *Dalton Trans.*, **48**, 5965 (2019).

Wha-Seung Ahn is a professor in the Department of Chemical Engineering, Inha University in Korea. He received his B.E., M.App.Sc., and Ph.D. (supervised by professor D.L.Trimm) from the University of New South Wales, Sydney, Australia. His current research is on catalysis and CO_2 capture using porous materials including zeolites, carbons, metal-organic frameworks, and porous organic polymers. He has published about 300 papers in international journals, and had represented Korea in the Inter- national Association of Catalysis Societies till 2020.